Light Water Reactor Sustainability Program

Complete Report on the Modeling of Precipitate Processes in Irradiated Reactor Pressure Vessel Steel March 31, 2017 Milestone

March 31, 2017

U.S. Department of Energy

Office of Nuclear Energy

Light Water Reactor Sustainability Program

Complete Report on the Modeling of Precipitate Processes in Irradiated Reactor Pressure Vessel Steel March 31, 2017 Milestone

Mahmood Mamivand (University of Wisconsin–Madison)
Huibin Ke (University of Wisconsin–Madison)
Shipeng Shu (University of Wisconsin–Madison)
Tam Mayeshiba (University of Wisconsin–Madison)
Dane D. Morgan (University of Wisconsin–Madison)

Key Collaborators
G. Robert Odette (University of California, Santa Barbara)
Peter B. Wells (University of California, Santa Barbara)
Nathan Almirall (University of California, Santa Barbara)

March 31, 2017

Prepared for the
U.S. Department of Energy
Office of Nuclear Energy

SUMMARY

This report has been assembled to address the following milestone due March 31, 2017:

Complete report on the modeling of precipitate processes in irradiated reactor pressure vessel steel

This milestone will focus on the application of cluster dynamics and machine learning methods for predicting hardening behavior as a function of alloy composition and radiation environment (flux, fluence, and temperature). We will integrate known hardening mechanisms and mechanical properties models into the cluster dynamics precipitate model and predict precipitation and hardening. We will also use machine learning methods on model and experimental hardening data to assess the ability of these methods to predict within existing data conditions (interpolation) and LWR life-extension conditions (extrapolation). The models will be validated and fit against UCSB data, which will include IVAR, ATR1, and ATR2 data. This milestone in conjunction with milestone M2LW-17OR0402013 of the High Fluence Effect on RPV Steels work package will fulfill the 2017 program milestone of "Provide validated model for transition temperature shifts in RPV steels".

This work was done in close collaboration with Professor G. R. Odette and his group at the University of California, Santa Barbara. The regular and strong interactions between all the participants in this collaboration has been critical to the development of this work and the content here represents intellectual contributions from the entire team.

ACKNOWLEDGEMENTS

This research was sponsored by the United States Department of Energy, Office of Nuclear Energy, for the Light Water Reactor Sustainability Research and Development effort.

CONTENTS

FIGURES

TABLES

ACRONYMS AND NOMENCLATURE

APT	Atom probe tomography
BCC	Body-centered cubic
CD	Cluster dynamics
CM6	Name of different alloy composition used by University of California, Santa Barbara, collaborators
CRP	Cu-rich precipitate
CV	Cross Validation
GKRR	Gaussian Kernel Ridge Regression
LC, LD, LH, LI, LG	Name of different alloy composition used by University of California, Santa Barbara, collaborators
LO	Leave-out
LWR	Light water reactor
KMC	Kinetic Monte Carlo
MNSP	Mn-Ni-Si rich precipitate
PIA	Post-irradiation annealing
RIS	Radiation-induced segregation
RMSD	Root mean square difference
RMSE	Root mean square error
RPV	Reactor pressure vessel
UMD	Unstable matrix defects

Complete Report on the Modeling of Precipitate Processes in Irradiated Reactor Pressure Vessel Steel

March 31, 2017 Milestone

1. INTRODUCTION

Reactor pressure vessels (RPVs) are permanent components in light water reactors (LWRs) and their irradiation embrittlement is one of the potential barriers to extending the lifetime of light water reactors. Therefore, predicting and having insight into the RPVs embrittlement in extended life conditions play a critical role in LWRs further licensing. In this report, we use two different approaches to model the RPVs embrittlement and gain insight into extended life conditions. We have primarily focused on developing a physics-based multiscale model to address the process of formation and growth of Cu-rich precipitates (CRPs) and Mn-Ni-Si-rich precipitates (MNSPs), which are the main causes of embrittlement in RPVs, under both irradiation and aging. We used the kinetic Monte Carlo technique for atomistic simulation, which gave us insight into early stages of Cu-Mn-Ni-Si precipitation and its morphological evolution. For continuum modeling, first we developed a Cluster Dynamics (CD) model for MNSPs which was capable of capturing the MNSPs evolution over the time scale of reactor lifetimes. Then we expanded the MNSPs CD model to include the effect of Cu. This model expansion is necessary as RPV steels essentially always have some potentially relevant level of Cu. The model of the coupling of Cu to MNSPs was informed by the kinetic Monte Carlo simulations. The CD model was benchmarked against high flux irradiation experimental data from the literature and UCSB and uncertain parameters (e.g. interfacial energy) were fitted to experimental data. The predictability of the CD model was tested by comparing the CD results against some new experimental data from ATR2 and good agreement was obtained. Then the model was used to gain insight into the embrittlement of RPVs under light water reactor (LWR) extended life conditions under which no experimental data is available. The CD model (with fitted parameters from irradiation experiments) were also validated against aging experimental studies at higher temperatures. The good agreement between modeling and experimental aging data supports the fidelity of fitted parameters for both irradiation and aging. We have also initiated a machine-learning-based approach, as opposed to a physics-based approach, to modeling the mechanical

response of RPVs. Here we report on preliminary investigations of machine learning for fitting and predicting changes in RPV yield stress.

2. EXECUTIVE SUMMARY OF MAJOR RESULTS

1. Kinetic Monte Carlo (KMC) simulation established a novel mechanism for precipitate growth that can explain the appendage morphology of Cu+MNSPs and may play a role in other multicomponent precipitates (see Sec. 4.1.2).
2. Qualitative and semi-quantitative models for Cu+MNSP evolution were developed which allow understanding of key mechanisms governing precipitate evolution and prediction of behavior trends under life-extension conditions (see Sec. 4.2). The uncertain parameters (e.g. interfacial energies) were fitted using the UCSB experimental data.
3. Cluster Dynamics (CD) modeling suggested that the alloy Ni content is the dominant compositional factor in forming MNSPs, while Mn and Si play lesser roles. The absolute threshold for MNSPs formation appears to be ≈ 0.5at.%Ni. The $\sqrt{f}$ of MNSPs at extended RPV life fluence of $10^{24}m^{-2}$ at 290°C can be fitted to a polynomial of alloy compositions, which can be used for quick estimation. The $\sqrt{f}$ versus T follows an approximately linear relation (see Sec. 4.2.1).The predictability of the Cu-MNS CD model was tested by using the new ATR2 experimental data and very good agreement was achieved (see Sec. 4.2.2.3).
4. The Cu-MNS CD model gave two key insights for LWR: 1) for high Cu bearing alloys most of available Cu in matrix precipitates out in the first couple of years of operation, 2) embrittlement continues to increase in extended life period due to the sluggish precipitation of MNS (see Sec. 4.2.2.4.2).
5. Machine learning using Gaussian Kernel Ridge Regression (GKRR) predicts the change in yield stress for compositions and conditions represented within the IVAR/IVAR+ database with a root-mean-square error (RMSE) of ~25 MPa. Cross-validation (CV) suggests little over-fitting (see Sec. 4.3).

3. METHODS

3.1 Kinetic Monte Carlo Simulations

3.1.1 The Kinetic Monte Carlo model

The KMC model is developed based on the framework of the model by Enrique and Bellon [1], and directly modified from the code developed by Shu et al. [2], adding multinary simulation capability and body-centered cubic (bcc) structural information.

A bcc rigid lattice is constructed from an N×N×N (N = 64 or 256) rhombohedral crystal with periodic boundary conditions. The faces of rhombohedron correspond to $\{110\}$ planes of the bcc crystal. Atoms migrate by thermally activated jumps, assisted by nearest-neighbor atom-vacancy exchanges. A single vacancy is introduced into the system. Nearest-neighbor atomic pair interactions (ε_{XY}) and atom-vacancy interactions (ε_{XV}) are used to model cohesion and vacancy formation energies of the system, and their fitting was discussed in previous reports. Homo-atomic pair interactions (i.e., interactions between atoms of the same chemistry) are estimated by assuming they are related to cohesive energies through $E_{coh}^{X} = \frac{Z}{2}\varepsilon_{XX}$, where Z is the nearest-neighbor site coordination number (Z = 8 for bcc structure). Hetero-atomic interactions (i.e., interactions between atoms with different chemistry) are defined through the ordering energy as $\omega_{XY} = 2\varepsilon_{XY} - \varepsilon_{XX} - \varepsilon_{YY}$. The value of ω_{XY} determines the shape of the binary X-Y phase diagram. Effective atom-defect pair interactions are used to reproduce the values of vacancy defect formation energies, defined as $E_{XV}^{f} = Z\varepsilon_{XV} - \frac{Z}{2}\varepsilon_{XX}$ [3].

The frequency of the thermal jumps is determined using standard rate theory. The attempt frequency is set to be a constant equal to $6\times10^{12}\,s^{-1}$, similar to the atomic vibration frequency. The activation energy is calculated using

$$E_a^X = E_0^{\mathrm{mig}} + E_a^{saddle}, \tag{1}$$

where E_a^{saddle} is the saddle-point energy. E_a^{saddle} is calculated using the final-initial-state energy (FISE) approximation, $E_a^{saddle} = \frac{E_f - E_i}{2}$, where E_i and E_f are the system total energies before and after the jump of the vacancy. The reference activation energy E_0^{mig} is assumed to be

dependent on the chemical species of the migrating atom, and the value of E_0^{mig} is taken from Ref. [4], by Messina et al.

During the simulation, time is incremented using a residence-time algorithm [5]. Since a single vacancy is introduced in the simulation cell, a fixed vacancy concentration is unphysically imposed. Thus, a rescaling of the KMC time t_{MC} is needed in order to obtain the physical time t that can be directly compared with the experiments. We follow the approach proposed by Nastar et al. [6] for the rescaling:

$$t = t_{MC} \frac{C_V^{KMC}(X)}{C_V^{irr}(X)}, \tag{2}$$

where $C_V^{KMC}(X)$ is the vacancy concentration in phase X, measured in KMC simulation, and $C_V^{irr}(X)$ is the radiation enhanced vacancy concentration in X phase, calculated according to Ref. [7].

3.1.2 Kinetic Monte Carlo Model Parameterization

The homo-atomic pair interactions ε_{XX} for determining E_i and E_f are determined from measured cohesive energies for bcc phase of the pure element. The hetero-atomic pair interactions ε_{XY} are obtained from molar excess free energies (G_{AB}^m), calculated by the CALPHAD method. Specifically, assuming a regular solution model one can write

$$G_{AB}^m = x_A G_0^A + x_B G_0^B + RTx_A \ln x_A + RTx_B \ln x_B + x_A x_B \Omega_{AB}, \tag{3}$$

where $\Omega_{AB} = \frac{Z}{2} N_A \omega_{AB}$. Ω_{AB} is available or can be fit from the CALPHAD model for G_{AB}^m and connects the CALPHAD output to the KMC input.

In previous milestones, we have described the details of the parameterization involving Fe, Mn, Ni and Si. In this milestone, we add Cu in the interactions, which were obtained from Ref. [8]. The complete interactions are listed in Table 1.

Table 1 The interaction parameters used in the simulation (all values are eV).

Ω_{AB}	Cu	Mn	Ni	Si
Fe	0.458	0.094	0.007	-1.542
Cu		0.090	0.106	-0.344

Mn		-0.465	-0.907
Ni			-1.850

Table 2. Cohesive energy of primary RPVs elements. [9]

Element	Fe	Cu	Mn	Ni	Si
$E_{cho}^{X}(eV)$	-4.28	-3.49	-2.92	-4.34	-4.03

3.2 Cluster Dynamics Simulations

3.2.1 Simulation Models

The models described in this section are mainly similar to what we described in the last milestone, except we have added a new nucleation mechanism on dislocations.

3.2.1.1 Basic Cluster Dynamics model

As described in previous milestones, the CD method [10-13] gives the size distribution of clusters by solving a series of ordinary differential equations as follows:

$$\frac{\partial f(n,t)}{\partial t} = \omega_{n-1,n}^{(+)} f(n-1,t) - \omega_{n,n-1}^{(-)} f(n,t) + \omega_{n+1,n}^{(-)} f(n+1,t) - \omega_{n,n+1}^{(+)} f(n,t), \quad (4)$$

where

$f(n,t)$ = concentration of clusters containing n atoms at time t.

The coefficient $w_{n,n+1}^{(+)}$ s are the rates at which clusters of size n absorb single atoms to grow to size n+1, $w_{n,n-1}^{(-)}$ s are the rates at which clusters of size n emit single atoms to shrink to size n-1, and $\Delta G(n)$ is the formation energy of clusters with n atoms. More details regarding this method can be found in Ref. [10-13].

For a system containing k precipitating components, the rates of absorption are given by:

$$\omega_{n,n+1}^{(+)} = \left[\sum_{i=1}^{j}\left(\frac{v_{i\alpha}^{2}}{\omega_{n_i;n_i+1}^{(+)}}\right)\right]^{-1}, \quad (5)$$

where

$w_{n_i,n_i+1}^{(+)}$ = rate at which clusters of size n gain one atom of species i.

The parameter $v_{i\alpha}$ accounts for the change in the composition of component i as the cluster grows from size n to $n+1$. It is defined by the following expression:

$$\nu_{i\alpha} = x_{i\alpha} + n\frac{dx_{i\alpha}}{dn}, \tag{6}$$

where

$x_{i\alpha}$ = atomic fraction of component *i* in clusters of size *n*.

Here it is assumed that $x_{i\alpha}$ does not change with *n*, thus $v_{i\alpha}$ equals $x_{i\alpha}$.

For diffusion-limited growth of the clusters, the absorption rate becomes:

$$\omega_{n,n+1}^{(+)} = 4\pi c_\beta a_\alpha D_{eff}^d n^{1/3}, \tag{7}$$

$$\frac{1}{D_{eff}^d} = \sum_{i=1}^{k} \frac{\nu_{i\alpha}^2}{x_{i\beta} D_i}, \tag{8}$$

where

C_β = total volume concentration of the particles of the different components in the ambient phase

$x_{i\beta}$ = molar fraction of the different components in the ambient phase.

The emission rate is given by:

$$\omega_{n+1,n}^{(-)} = \omega_{n,n+1}^{(+)} \exp\left(\frac{\Delta G(n+1) - \Delta G(n)}{k_B T}\right), \tag{9}$$

where

ΔG(n) = formation energy of clusters with *n* atoms from the matrix, which can be written as:

$$\Delta G(n) = n(g_p - \sum_i x_i \mu_i) + \sigma(n), \tag{10}$$

where

g_p = free energy per atom of the precipitate phase

μ_i = chemical potential of component I in the matrix

$\sigma(n)$ = interfacial energy of a cluster of size *n*.

With this form, the difference *ΔG(n+1)-ΔG(n)* reduces to:

$$\Delta G(n+1) - \Delta G(n) = g_p - \sum_i x_i \mu_i + [\sigma(n+1) - \sigma(n)], \tag{11}$$

The chemical potentials can be written as:

$$\mu_i = \mu_i^0 + kT[ln\gamma_i + lnc_i], \tag{12}$$

Where γ_i is the activity coefficient. When the matrix phase is in equilibrium with the precipitate phase we have the relationship:

$$g_p - \sum_i x_{i\alpha}\mu_i = 0$$
$$g_p - \sum_i x_{i\alpha}[\mu_i^0 + kTln\gamma_i] = kT\sum_i x_{i\alpha} ln\overline{c_i} \quad (13)$$

In dilute alloys, the γ_i in Eq. (13) will become constant according to Henry's law, thus according to Eq. (11) - (13), we can obtain

$$\Delta G(n+1) - \Delta G(n) = kT\sum_i x_{i\alpha} ln\frac{\overline{c_i}}{c_i} + [\sigma(n+1) - \sigma(n)], \quad (14)$$

Substituting Eq. (14) into Eq. (9), the emission rate can be written as:

$$\omega_{n+1,n}^{(-)} = \omega_{n,n+1}^{(+)} \frac{\overline{\prod_i c_i^{x_i}}}{\prod_i c_i^{x_i}} \exp\left(\frac{\sigma(n+1)-\sigma(n)}{k_B T}\right), \quad (15)$$

where $\prod_i c_i^{x_i}$ and $\overline{\prod_i c_i^{x_i}}$ are the solute product and solute product at equilibrium, respectively, and they are represented by K_{sp} and $\overline{K_{sp}}$, respectively.

The distribution function f(n=1,t) at n=1 is described as:

$$f(n=1,t) = c_\beta \prod_{i=1}^{k} x_{i\beta}^{x_{i\alpha}} , \quad (16)$$

3.2.1.2 Heterogeneous nucleation

In our previous milestone, we showed that homogeneous nucleation is inadequate to match the experimentally observed MNS precipitates number density in Cu-free alloys and some form of in-cascade MNS precipitation is needed. Similarly, Monte Carlo simulations [14] show Cu will precipitate in cascade in FeCu binary alloys. In addition to in-cascade precipitation, formation of Cu and Cu-MNS precipitates on dislocations have been observed both in experiments [15] and simulations [16]. These results suggest the need for both in-cascade and on dislocation heterogeneous dislocation in addition to homogeneous nucleation. Heterogeneous nucleation at grain boundaries was not considered in the present study because the number of grain boundary nucleation sites are much smaller than those associated with cascades and dislocations for RPVs and will make a negligible contribution to high-fluence precipitate number densities.

3.2.1.2.1 Nucleation in cascade

For nucleation in cascade the precipitates nucleation rate is proportional to cascade production per atom $\sigma_{cas}\theta/\Omega$ (irradiation term) and ratio of the instantaneous solute product to reference solute product, $K_{sp}(t)/K_{sp}^0$ (thermodynamics term). For simplicity we assume that cascades produce only one size precipitates. Therefore, the nucleation rate in cascade is

$$R_{het}(n_{het}, t) = \alpha \cdot \sigma_{cas}\theta/\Omega \cdot K_{sp}(t)/K_{sp}^{0}$$
$$\text{And } R_{het}(n \neq n_{het}, t) = 0 \tag{17}$$

where α is cascade cluster production efficiency factor, σ_{cas} is the cascade production cross section, θ is the neutron flux, and Ω is the atomic volume, $K_{sp}(t)$ is instantaneous solute product and K_{sp}^{0} reference solute product.

With the cascade induced nucleation the general equation for cluster dynamics becomes:

$$\frac{\partial f(n,t)}{\partial t} = R_{het}(n,t) + \omega_{n-1,n}^{(+)} f(n-1,t) - \omega_{n,n-1}^{(-)} f(n,t) + \omega_{n+1,n}^{(-)} f(n+1,t) - \omega_{n,n+1}^{(+)} f(n,t) \tag{18}$$

3.2.1.2.2 Nucleation on dislocation

It is known that dislocations are favorable nucleation sites for second phase precipitation because precipitate formation on dislocation releases the excess free energy associated with the dislocations [17]. To account the effect of dislocations on nucleation we combine the CD model with the theory of heterogeneous nucleation on dislocations that was originally developed by Cahn [17]. Considering the effect of dislocation nucleation on CD model the Eq. (10) will be,

$$\Delta G(n) = n(g_p - \sum_i x_i \mu_i) + \sigma(n) + \Delta G_{disl}(r_p), \tag{19}$$

where the last term corresponds to the released excess free energy associated with the nucleation of a precipitate on dislocation and can be given as [17],

$$\Delta G_{disl}(r_p) = \begin{cases} \int_{-r_p}^{r_p} [E_{core}]dl, & r_p < r_{core} \\ \int_{-r_p}^{r_p} [E_{core} + \dfrac{\mu b^2}{4\pi} \ln(\dfrac{r(l)}{r_{core}})]dl, & r_p > r_{core} \end{cases}, \tag{20}$$

where r_{core} and E_{core} are respectively the dislocation core radius and core energy, r_p is the precipitate radius, r is the distance between a point on the precipitate interface and the dislocation line, l is the distance from the center of a precipitate along the dislocation line, and μ is elastic shear modulus.

Considering the typical size of Cu-MNS precipitates in RPVs (~2-3 nm) we approximate that no precipitate would nucleate within a distance of 3 nm from any evolving precipitate to avoid precipitates overlap.

Table 3 Parameters used in CD model of nucleation on dislocation.

Dislocation core radius (r_{core}, nm)	0.4 [18]
Dislocation core energy (E_{core}, eV/Å)	0.937 [18]
Burgers vector (b , nm)	0.248 [19]
Atomic volume (Ω_a, m^3)	1.18×10^{-29}
Elastic shear modulus (μ , GPa)	80 [19]
Dislocation sink strength (dislocation density) (ρ , m^{-2})	2×10^{14} [7]

3.2.1.3 Radiation enhanced diffusion (RED) model

The radiation enhanced diffusion (RED) model used here is based on that developed by Odette et al. [7]. The radiation enhanced diffusion coefficients are expressed as

$$\mathrm{D}^{irr} = D_v X_v \frac{D^{th}}{D^{sd}} + D^{th}, \tag{21}$$

where D^{irr} is the diffusion coefficient under irradiation, D_v is the diffusion coefficient of vacancies, X_v is the vacancy concentration under irradiation, D^{th} is the solute thermal diffusion coefficient of solute under thermal aging condition, and D^{sd} is the self-diffusion coefficient of Fe in the matrix.

Defect conservation balances, treating vacancy and SIA production, transport and fate, were used to establish the steady-state vacancy concentration (X_v) under irradiation, which can be expressed from rate theory models as a function of the fraction of vacancies and self-interstitials (SIA) that escape recombination and reach fixed dislocation sinks (g_s), which is given as:

$$X_v = \frac{g_s \xi \sigma_{dpa} \phi}{D_v S_t}, \tag{22}$$

Here, φ is irradiation flux, σ_{dpa} is the displacement-per-atom (dpa) cross-section, ξ is the fraction of vacancies and SIA created per dpa. Assuming that defect recombination occurs as vacancies and SIA diffuse freely through the ferrite matrix it can be shown that

$$g_S = \frac{2}{\eta}\left[(1+\eta)^{1/2} - 1\right], \tag{23}$$

$$\eta = \frac{16\pi r_v \xi \sigma_{dpa} \phi}{\Omega_a D_v S_t^2}, \tag{24}$$

Here, r_v is the SIA-vacancy recombination radius, Ω_a is the atomic volume, and S_t is sink strength.

We will assume that the precipitate growth is dominated by vacancy mediated diffusion of solutes to the precipitates, so correct modeling of the vacancy concentrations and associated RED is critical. Vacancy fates include clustering, annihilation at sinks and recombination with SIA. The dominant fixed sinks for vacancies are typically dislocations in RPVs. However, UMDs also act as vacancy sinks and can be dominant at very high flux. Furthermore, recombination will be greatly enhanced if vacancies are strongly bound to these UMDs. Odette et al.[7] have built a model to include the effect of UMD in the recombination-dominated regime under very high irradiation flux. This irradiation flux effect can be simply described by adjusting g_s by a scaling law as

$$g_s(\phi) \approx g_s(\phi_r)\left(\frac{\phi_r}{\phi}\right)^p, \tag{25}$$

Here, φ_r is a reference flux and p is a scaling exponential factor. The effective p starts at 1 in the thermal diffusion dominated regime at very low flux; p is 0 in the sink-dominated regime and p=0.5 in the recombination-dominated regime. The p again approaches 1 at high flux in the UMD sink-dominated regime. We will use this scaling law expression in our model to effectively include the effects of UMDs on the vacancy concentrations.

3.2.2 Parameters for the MNSP Cluster Dynamics model

All the parameters used in the cluster dynamics model for MNSPs are given in this section, and most of them are the same as were reported in the last milestone. The only differences are the reference solute product and heterogeneous nucleation generation rate coefficient in Sect. 3.2.1.2.1. Instead of choosing 0.01 as the reference solute product, 2.4×10^{-3} is chosen, as a result the heterogeneous nucleation generation rate coefficient has been changed to 7.2×10^{-3} from 0.03, so that their ratio stays the same. As can be seen from Eq. (16), the model stays the same as long as the ratio between reference solute product and heterogeneous nucleation generation rate coefficient doesn't change. The purpose of this change was so that the reference solute product is close to the equilibrium solute product around 290°C (in Table 4), which allows us to interpret

the heterogeneous nucleation generation rate coefficient as the number of MNS clusters that will be generated per cascaded in the equilibrium state. The equilibrium solute products of the two phases studied at different temperatures are obtained from the TCAL2 database [20]. These equilibrium solute products at different temperatures are listed in Table 4. Note that the equilibrium solute product here for T6 are calculated with composition of 51.1%Ni-33.3%Mn-15.6%Si, since for the alloys studied here the predicted equilibrium compositions of T6 vary over a Ni composition of just 51%-52%.

Table 4 Equilibrium solute product for each phase at different temperatures

Temperature (°C)	Equilibrium solute product ($\times 10^{-3}$)	
	T3	T6
280	1.96	2.33
284	2.12	2.53
290	2.21	2.56
300	2.45	2.82
400	6.26	6.57
425	7.86	7.95

The thermal diffusion coefficients of Mn, Ni, Si and Fe in ferromagnetic Fe used in this paper are summarized in Table 5.

Table 5 Diffusion coefficients under thermal condition.

Element	D_0 (cm^2/s)	Q (kJ/mol)	Reference
Mn	1.49	234.0	[21]
Ni	1.4	245.6	[22]
Si	0.78	231.5	[23]
Fe	27.5	254.0	[24]

All other parameters are listed in Table 6. Most of them are obtained from two papers [7, 25]. Four of them, heterogeneous nucleation size and rate coefficient (see Sec. 3.2.1.2) and two interfacial energies are fitting parameters. These parameters were fitted to 28 experimental data points of precipitate number density, mean radius and volume fraction for alloys under different irradiation conditions by mapping a fine grid of the values of these parameters in reasonable range, and the optimal set of parameters were obtained for parameter values where the smallest

root mean square difference (RMSD) between simulation results and experimental data was realized.

Table 6 Parameters used in calculating radiation enhanced diffusion coefficient and other parameters.

SIA – vacancy recombination radius (r_v, nm)	0.57 [7]
Fraction of vacancies and SIA created per dpa (ξ)	0.4 [7]
Displacement-per-atom (dpa) cross-section (σ_{dpa}, m^2)	1.5×10^{-25} [7]
Atomic volume (Ω_a, m^3)	1.18×10^{-29}
Vacancy diffusion coefficient pre-exponential factor (D_v, m^2s^{-1})	1×10^{-4} [25]
Vacancy migration energy (E_v^m, eV)	1.3 [25]
Dislocation sink strength (dislocation density) (ϱ, m^{-2})	2×10^{14} [7]
Flux effect scaling exponential factor (p)	0.2 [26]
Cascade cross section ($\sigma_{Cascade}$, m^2)	2×10^{-28} [26]
Reference solute product (K_{sp}^0)	2.4×10^{-3}
Heterogeneous nucleation size (n_h) (FITTED)	60
Heterogeneous nucleation generation rate coefficient (α) (FITTED)	7.2×10^{-3}
Interfacial energy of T3 phase (σ_{T3}, J/m^2) (FITTED)	0.190
Interfacial energy of T6 phase (σ_{T6}, J/m^2) (FITTED)	0.175

3.2.3 Coupling Cu to Mn-Ni-Si precipitation

Formation of pure Mn-Ni-Si precipitates (MNSPs) in RPV steels is limited to Cu-free or very low Cu bearing (Cu<0.06at.%) alloys. However, there exist some level of Cu in major in-service RPV steels and its concentration can reach up to 0.25at.% [27]. In the presence of Cu, it is seen that MNSPs are usually spatially correlated with Cu-rich precipitates (CRPs) in RPV steels [28-32]. Note that here we define a CRP as a primarily Cu containing precipitate, but one that also includes other solutes (e.g., a Cu core with Mn, Ni and Si atoms coating it). In section 3.2.1, we described the general cluster dynamics model for single and multicomponent precipitates formation and we parameterize it for MNSPs in Cu-free (Cu<0.06at.%) steels in section 3.2.2. In this section, we expand the CD model to treat the precipitation of Cu along with Mn-Ni-Si. The coupling of Cu and MNSPs is necessary to fully understand their combined impact on the embrittlement of RPV steels

Based on KMC results (sections 4.1) and test reactor data [33-35] we know that CRPs will form in alloys containing more than ~0.06 at.% Cu. The mechanism for formation of CRPs in the presence of MNS is still being explored, but from atom probe observations [36] and our KMC simulations, we propose that the mechanism is as follows. In the early stages of irradiation, Cu clusters precipitate out, then the Mn, Ni, and Si move toward Cu precipitates and coat the Cu precipitates in just a monolayer or so of Mn, Ni, and Si, forming CRPs. The CRPs enrichment in these solutes can be understood and modeled within the framework of both classical thermodynamics [37] and atomistic simulations [14] (section 3.1). As the irradiation continues the Cu depletes in the matrix (due to its very low solubility limit) while Mn-Ni-Si are still supersaturated. During the Cu precipitation and after, Mn, Ni, and Si continue to precipitate out on the CRP, forming an appendage morphology of a well-developed MNSP, which is discussed in detail in section 4.1.

The above process of coupling Cu and Mn-Ni-Si precipitation is highly complex, and all the features could not be readily incorporated into a practical model. Instead, we took an approximate approach that built separate Cu and MNS precipitate models, and then coupled them in a simple manner that mimicked the essence of the above processes, while simultaneously requiring relatively few adjustable parameters (as illustrated schematically in Figure 1). The right branch of Figure 1 shows the MNSP model, uses the theoretical approach from Sec. 3.2.1 and whose parameters are given in Sec. 3.2.2. The left branch of Figure 1 shows the Cu precipitation model. This model uses the same theoretical approach as described in Sec. 3.2.1, although all of the formalism for multiple species is simplified to just Cu. The parameters for this model are given in Sec. 4.2.2.1. Finally, the coupling of Cu and MNS precipitation is shown schematically by the middle branch of Figure 1. This portion is quite new and we describe it in some detail here as well as Sec. 4.2.2.1.

We coupled the Cu and MNSP by assuming that during the Cu nucleation stage any Cu precipitate which has 20 atoms (~Cu precipitate critical size) or more has an accompanying MNSP that has a size proportional to the Cu precipitate. This effectively co-nucleates a MNSP with the Cu precipitate. The MNSP is a distinct precipitate from the Cu precipitate in the model, but does not grow independently during the this co-nucleation phase as it is pinned to the Cu precipitate size. The ratio of MNSP to Cu precipitate size during this co-nucleation stage is a fitting parameter. When the Cu nucleation stops, we decouple the co-nucleation and let the Cu

and MNSP grow separately. The Cu growth after this stage is limited due to the significant Cu depletion in the matrix, but MNSPs continue to grow, which represents the appendage growth. This way of coupling Cu to MNSP is a quite severe approximation and leaves out many features of our understanding of the true mechanism of precipitation described above. Perhaps the most dramatic feature of the approximation is that we replace the complex process of Mn, Ni, and Si segregating to the Cu/Fe interface and then growing as an appendage with a single nucleation event of an MNSP separate from the Cu precipitate. This approximation still captures the key role of Cu catalyzing the nucleation and growth of MNSPs but greatly simplifies the process in ways that may impact the fidelity of the predicted MNSP evolution. The atom probe experiments and KMC simulations show that Cu precipitates are coated with Mn, Ni, and Si atoms, which means the Cu precipitate is really a CRP, and CRPs will have a different interfacial energy than pure Cu precipitates and pure MNSP. Therefore, we considered the interfacial energy of CRPs (Cu clusters bigger than 20) to be the average of a Cu and MNSP interfacial energy. We note that we tested the sensitivity of the results to this parameter and found very little variation in results by shifting this number between Cu interfacial energy to MNSP interfacial energy. At this stage we assess the impact of the model approximations by determining to what extent we can model a large body of Cu+MNSP evolution data, and the relatively good success we have compared to the experimental data (see Sec. 4.2.2) supports that our approach has captured the essential elements of the Cu+MNSP coupling..

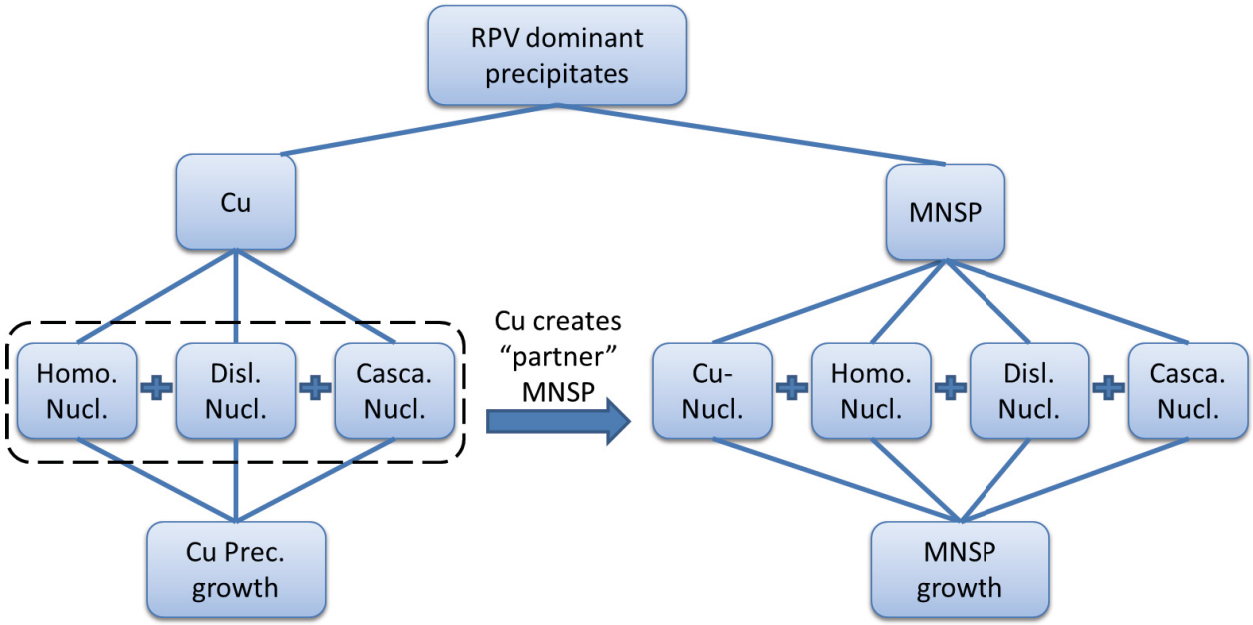

Figure 1. A flowchart of precipitate formation in RPVs in the presence of Cu.

3.3 Machine Learning

3.3.1 Introduction

In addition to the physics based methods pursued above, we have also used machine learning and data mining to produce a generalizable model for predicting the effect of irradiation on RPV hardening. Previously, Castin et al. used artificial neural network (ANN) techniques to model hardening based on the RADAMO database (SCK•CEN), with a mean predictive error of 45 MPa; however, they note that there is room for improvement of the extrapolative ability of the model, particularly as the principal composition variables ended up being only Cu and Ni content, and the elemental compositions in the database did not vary independently.[38] Kemp et al. similarly used ANN to model and predict yield stresses based on published irradiated steel data taken over a wide-range of temperatures, and had quite large errors in their model. The authors noted that the high errors for some dose rate and temperature ranges could be improved with additional data; that particular strengths of the model were its generalizability over alloys and its ability to give uncertainty estimates, which could then inform selection of additional data points for experiment; and that additional modeling approaches which could incorporate known physics could be complementary.[39] Our analysis is distinct from previous work in that it is

using a very extensive dataset that is more focused on data relevant for RPV steels, including a more restricted composition range and temperature range than some of the above studies, and we are using a somewhat different set of approaches.

To complement the previous ANN studies, this model uses a conceptually simpler Gaussian Kernel Ridge Regression (GKRR) model, requiring optimization of only two hyperparameters, along with physically based and empirically based descriptors taken from literature.[7, 40] The reusable model framework builds in the capability to handle unknown high fluence and high flux effects: because the model is validated independently on a modeled cluster dynamics dataset, it can be reapplied to produce different model forms as more data and descriptors become available. Additional data would take the form of more high fluence surveillance and test data points. Additional descriptors may be identified and added due to improved high fluence and flux understanding.

3.3.2 Model introduction

We develop a generalizable machine-learning model using the information available from the IVAR database, namely the elemental compositions of Cu, Ni, Mn, Si, P, and C, irradiation temperature, flux, and fluence, with hardening in MPa as the response. Flux and fluence are combined into any number of effective fluences,[7] each defined by a *p*-value.

Gaussian Kernel Ridge Regression (GKRR) implemented through the Python[41] package scikit-learn,[42] produces a model from these descriptors. The radial basis function (RBF, or Gaussian) kernel determines the distance between feature vectors, and is characterized by hyperparameter γ, where the value of the kernel $K(x, y) = \exp(-\gamma \|x - y\|^2)$, where small values of γ increase the tolerance of what feature vectors are considered similar, and the weighting induced by the kernel is smoothed out over a larger area of feature space. Ridge regression performs linear regression in the kernel and data space (which will be a non-linear function in original space when using a non-linear kernel) and uses the hyperparameter α as the coefficient of the L2 norm penalty in the ridge regression. The hyperparameter α can decrease the sensitivity of the fit to random error in cases where the descriptors have some interdependence, with larger α allowing less sensitivity and penalizing large coefficients.

From experimental IVAR and IVAR+ data provided, we make the following changes:

- Removal of alloy LO, which has identical composition and data as alloy LC but was annealed for different times than other alloys in the database.
- Removed duplicate entries (i.e., entries for the same alloy, flux, fluence, and temperature), with the lower hardening response removed, leaving the larger hardening response. The lower hardening response is typically for an alloy that has been annealed for different times than other alloys in the database.
- Updated the irradiation temperature for alloys CM6, LC, LD, LG, LH, and LI at a flux of $2.3x10^{14}$ n/cm^2/sec and a fluence of $1.1x10^{21}$ n/cm^2 from 290°C to 320°C after communication from UCSB (this change is due to the change in temperature recently reported for all the so-called ATR1 irradiations).

3.3.3 Model details

As described above, the available data for regression consists of the elemental compositions of Cu, Ni, Mn, Si, P, and C, irradiation temperature, flux, and fluence, with hardening in MPa as the response. From this data, the descriptors used for regression are as follows, although the regression method described below could be reapplied to different or extended sets of descriptors.

- Atomic percent values of Cu, Ni, Mn, Si, P, and C as reported by the alloy compositions in weight percent. Fe is assumed to be the remainder of the weight balance after the six elements described above.
- Irradiation temperature
- Effective fluence, as calculated from the method in Odette et al.,[7] using a p-value of 0.2, consistent with Section 3.1 and 3.2. Because the range of effective fluence spans several orders of magnitude, this descriptor is considered on a logarithmic scale.

Each descriptor is normalized linearly over the total set of training and testing data, using the formula $(x - min)/(max - min)$. In the future, the training data and the testing data may come from two different datasets, for example, training on IVAR conditions and testing on LWR conditions. Currently, training and testing data comes solely from the experimental IVAR+ data.

Hyperparameters α and γ are currently optimized through a simple grid search evenly distributed over log space, with twenty points each in the range of (-6,0) for alpha and (-1.5 to

1.5) for gamma. In the future, a genetic algorithm method may be used to optimize the hyperparameters and potentially also the number and value of *p*-values for effective fluence descriptors.

4. RESULTS

4.1 Kinetic Monte Carlo Simulation of Co-precipitation of Cu-MnNiSi Precipitates

4.1.1 Morphological characteristics of Cu-MnNiSi precipitates

This section describes an APT data set showing the commonly observed Cu+MNSP appendage morphology, whose explanation has been the focus of our kinetic Monte Carlo simulations. A high-Ni, Cu-bearing steel named LD (0.25 at.% Cu, 1.18% Ni, 1.08% Mn, 0.54% Si) was neutron irradiated at ≈ 290 ˚C to fluences (E > 1 MeV) of 6.3×10^{19} n-cm^{-2} and 1.4×10^{20} n-cm^{-2} at fluxes of 1.0×10^{14} n-cm^{-2}s^{-1} and 3.6×10^{12} n-cm^{-2}s^{-1} in the Belgian Reactor 2 (BR2) and the US Advanced Test Reactor (ATR), respectively. APT samples were prepared using the focused ion beam lift-out method and run in a LEAP 3000X HR at the University of California, Santa Barbara. The samples were analyzed at 50K with a pulse fraction of 20% of the standing voltage and a 0.3-0.5% detection rate. Data reconstruction and analysis was performed in the Integrated Visualization and Analysis (IVAS) software. The plane spacing in either (200) or (110) poles was used to scale the reconstructions. The cluster analysis was performed using the cluster search tool in the IVAS software with order = 5 and d_{max} = 0.5-0.6 nm.

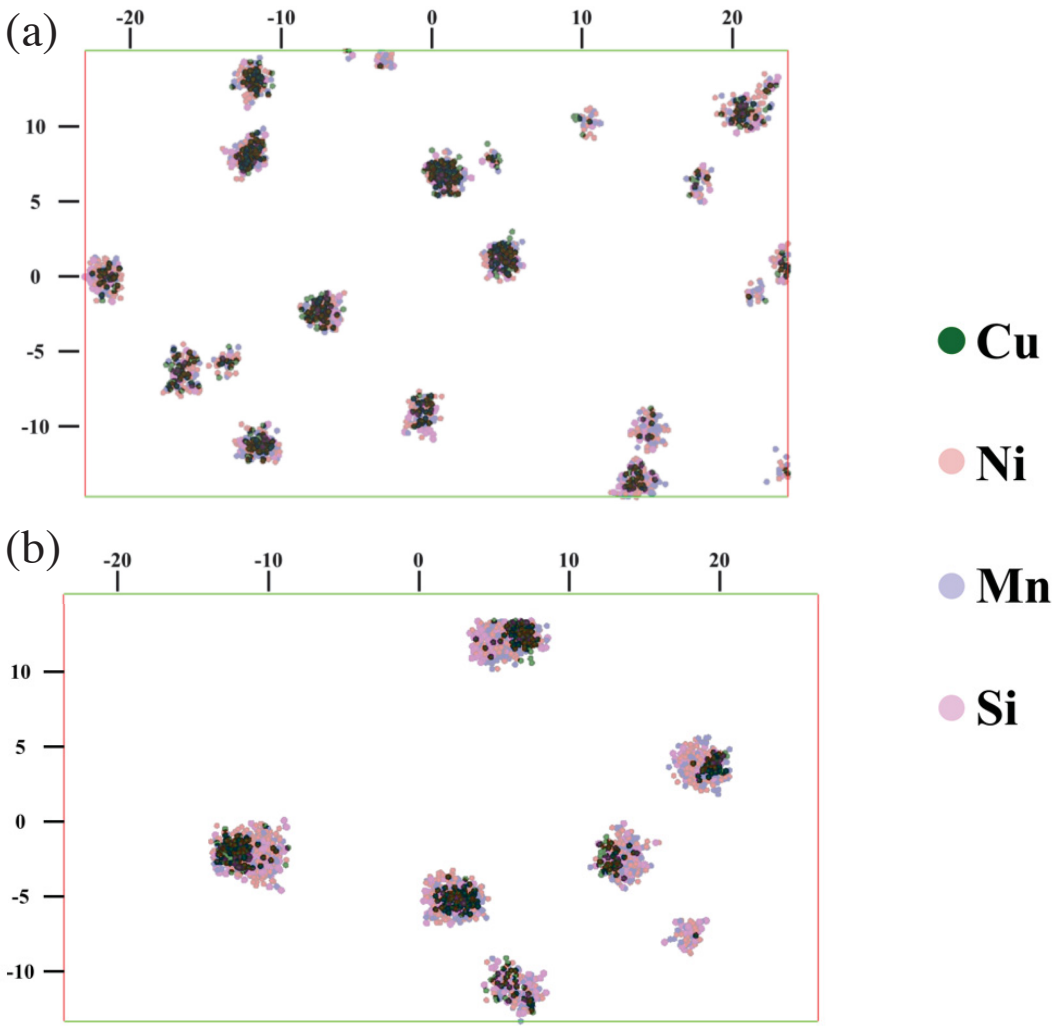

Figure 2 atom maps from (a) the BR2 irradiation and (b) the ATR irradiation showing Cu atoms in green and Mn, Ni and Si atoms as partially transparent to more clearly see the precipitate morphology.

Example atom maps are shown in Figure 2 for the (a) lower fluence BR2 and (b) higher fluence ATR conditions. Note that the Mn, Ni and Si atoms were made partially transparent to more clearly show the precipitate morphology. The precipitates in the lower fluence BR2 condition are much more numerous and smaller ($N = 9.5 \times 10^{23}$ m^{-3}, $\langle r \rangle = 1.1$ nm) than in the ATR condition ($N = 5.7 \times 10^{23}$ m^{-3}, $\langle r \rangle = 1.6$ nm). Note that the difference in the precipitate N and $\langle r \rangle$ is likely caused by both the lower fluence in the BR2 condition as well as the higher flux. The results here are consistent with previous experiments that have shown higher neutron flux results in smaller, more numerous precipitates at a given fluence [43]. The BR2 sample shows

precipitates that are predominantly Cu with slight enrichments of Mn, Ni and Si. In addition, a core/shell structure can be observed that is consistent with previous studies [8, 44, 45]. At higher fluence, the precipitates have almost doubled in size as is seen in Figure 1(b). The precipitated Cu is approximately the same as the lower fluence condition, meaning that the precipitate growth has primarily been caused by the addition of Mn, Ni and Si atoms. Here, the Mn, Ni and Si no longer only form a shell around the Cu core, but also have an almost pure Mn-Ni-Si appendage on one side of the CRP. The origin of this precipitate morphology has not previously been reported and thus is the focus of modeling in the following sections.

4.1.2 KMC simulation of the nucleation and growth of the Cu-MnNiSi precipitates

In the LKMC simulations, a five-component alloy, containing Fe, Cu, Mn, Ni and Si, was constructed on a rigid body-centered cubic lattice with a composition that corresponds to the LD alloy (see Section. 4.1.1). Atomic interactions are modeled using the pairwise interaction energies ε_{ij}, i, j = Fe, Cu, Mn, Ni, Si, given in Table 1.

The parameterization of the LKMC simulation has been validated by simulating post-irradiation annealing of the MnNiSi phase, and showed impressive agreement with the post-irradiation annealing results [46], reproducing the observed evolution of volume fraction, f_v, precipitate number density, N, and mean radius, $\langle r \rangle$. The details have been given in previous reports and are not shown again here.

Figure 3(a) is a snapshot of the LKMC simulation and shows the model reproduced the same Cu-MnNiSi appendage morphologies as was observed experimentally (see Figure 2). The Cu clusters and MnNiSi phase form co-precipitates, with Cu clusters largely visible at the edge of the whole precipitates. A magnified precipitate is shown in Figure 3(b), in which two isoconcentration surfaces were constructed to show a clearer boundary of the Cu cluster and the Cu-MnNiSi co-precipitate. Figure 3(c) shows a 1-dimensional compositional profile along the direction of the arrow. The peaks representing the Cu cluster and the MnNiSi phase can be clearly distinguished, showing the asymmetric positioning of the Cu cluster. Note that in the simulation, the MnNiSi phase is an ordered B2 structure, in which Ni and Mn occupy two sublattices, with Si randomly replacing some Mn atoms. This bcc-based ordering state is believed to be probable at the early stage of the precipitation, when the precipitates are coherent with the Fe matrix. When the precipitates grow to larger sizes, the structure of MnNiSi phase is

likely to transform to that of the G-phase, as characterized by synchrotron-based x-ray diffraction [47]. Nevertheless, the precipitate structure predicted by our LKMC simulation captures the fact that the ordered MnNiSi precipitate has a lower free energy level compared to the disordered counterpart.

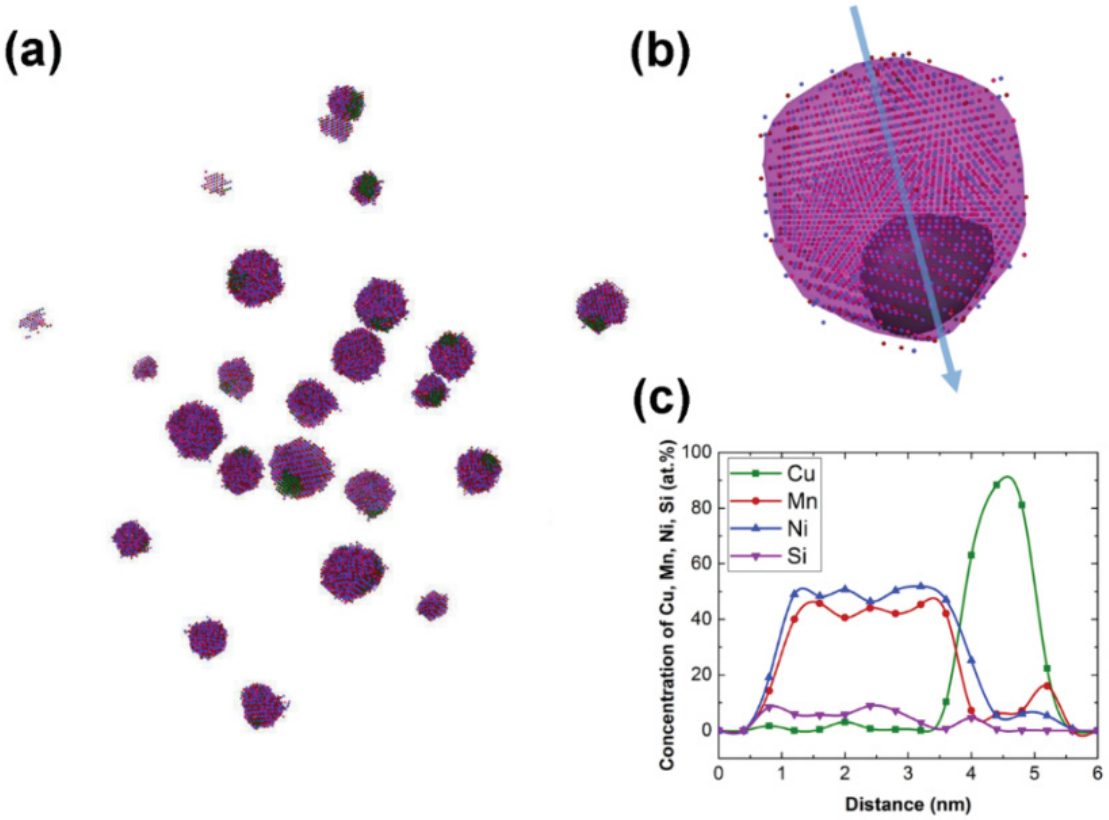

Figure 3 (a) a snapshot of the LKMC simulation, showing the microstructure of the simulated alloy (b) a magnified Cu-MnNiSi precipitate, with iso-concentration surfaces to clearer show the structure of the precipitate (c) a 1-D composition line scan of the precipitate.

A unique advantage of the LKMC simulation over present experimental characterization methods is that it can track one particular precipitate and identify its detailed temporal evolution. Figure 4 is a sequence of snapshots of a typical Cu-MnNiSi co-precipitate, showing the temporal evolution of the microstructure. At the early stages of formation, seen in Figure 4(a), the precipitate has a copper-rich core, with Mn, Ni and Si atoms coating it, the latter of which are stabilized by their ability to lower the Cu-Fe interfacial energy [48]. In the early stage of the growth regime, see Figure 4(b-c), more Cu, Mn, Ni and Si atoms diffuse to the precipitate. The MnNiSi phase preferentially grows on one side of the whole precipitate. At later stages of growth, Figure 4(d-e), as the Cu atoms in the matrix deplete, the growth of the Cu-MnNiSi

precipitate is mainly driven by incorporating Mn, Ni and Si atoms, forming an ordered B2 phase as an appendage on the Cu-rich portion. Over time, the simulation evolves to reproduce a MnNiSi appendage structure that is nearly indistinguishable from that observed in APT experiments.

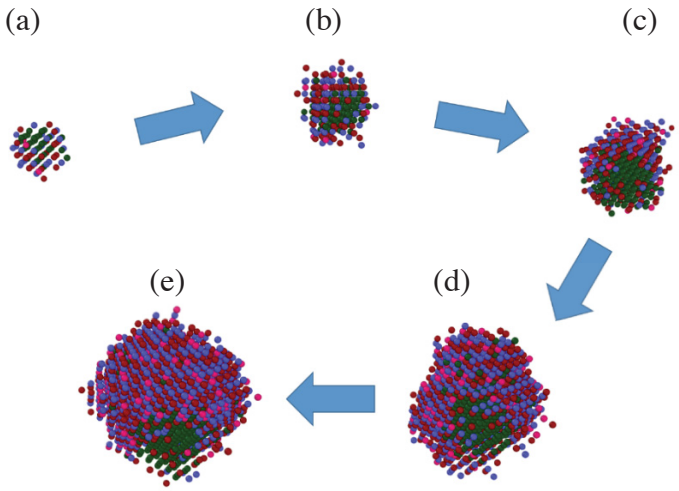

Figure 4 Temporal evolution of the Cu-MnNiSi precipitate reproduced by LKMC simulations. (a) Formation of a Cu cluster coated by a layer of MnNiSi (b) and (c) nucleation of MnNiSi ordered phase on the Cu cluster (d) and (e) further growth of the MnNiSi ordered phase, note that the Cu cluster is always on the edge of the whole precipitate.

To elucidate the mechanism of the asymmetric growth of the MnNiSi phase, detailed analysis of the simulated microstructure was performed. First, the trajectory of the center of mass (COM) of both the Cu cluster and the whole precipitate is plotted for a typical Cu-MnNiSi precipitate in Figure 5(a). The black trajectory, which shows the movement of the COM of the whole precipitate, is very short during the growth of the precipitate, indicating an isotropic growth rate in all the radial directions. However, the blue trajectory, which tracks the movement of the COM of the Cu precipitate, shows a clear absolute displacement toward one direction, away from the COM of the whole precipitate. Figure 5(b) shows the distance between COMs of the Cu and the whole precipitate along with the radius of the whole precipitate. This demonstrates that as the precipitate grows, the COM of the Cu and whole precipitate move further and further apart, which would be expected for an appendage growth where Cu is always on the edge of the precipitate.

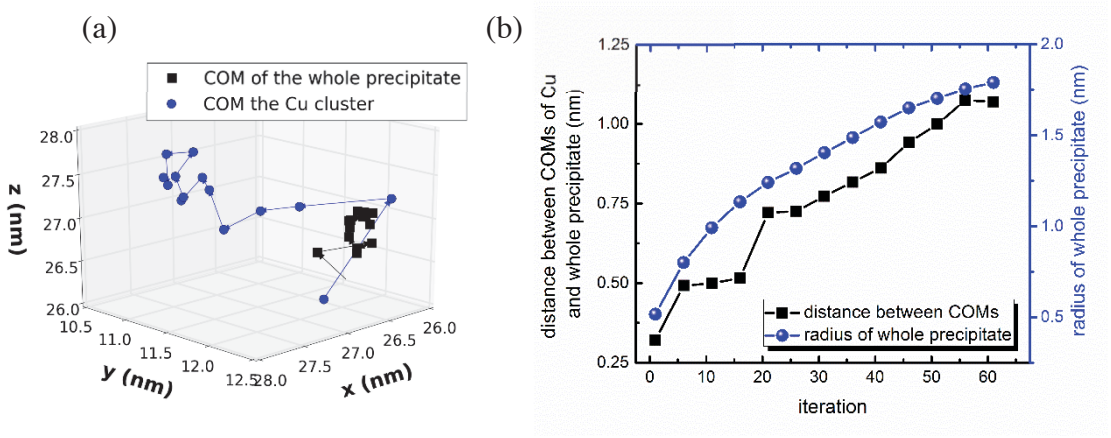

Figure 5 (a) Movement of the center of mass (COM) of the whole precipitate compared to that of the Cu cluster (b) Distance between COMs as the precipitate grows, plotted for the largest precipitate in the system. The radius of the whole precipitate is also plotted to show that the distance between COMS is directly correlated to size of the Cu-MnNiSi precipitate.

4.1.3 Discussion on formation mechanism of MNS appendage

The formation of the MnNiSi appendage structure is somewhat unexpected, in particular because it results in the formation of a high-energy Cu/Fe interface. Intuitively one would expect a core-shell structure to form, removing the high-energy Cu/Fe interface but having a Cu core with a MnNiSi shell with a low MnNiSi/Fe interfacial energy. Thus, it is important to identify the thermodynamic and kinetic factors that lead to this morphology. It has been demonstrated both experimentally and computationally that in the early stages of Cu precipitation in the high-Ni alloy, the clusters have a Cu-rich core with the relatively slow-diffusing Mn, Ni and Si atoms enriching the Cu/Fe interface and forming a thin coating layer. However, at the later stages of the precipitation process, as Cu depletes in the matrix, the MnNiSi phase preferentially grows on one side of the Cu core.

To investigate the key factors that control the formation of the MnNiSi appendage morphology, both possible thermodynamic and kinetic contributions will be assessed. Thermodynamically, three interfacial energies, $\gamma_{\text{Fe-Cu}}$, $\gamma_{\text{Fe-MnNiSi}}$ and $\gamma_{\text{Cu-MnNiSi}}$, are important for this precipitation process. As a result of the large driving force for phase separation and faster kinetics, Cu precipitates out of the solution rapidly, forming a high density of small Cu clusters. If there is sufficient Cu to rapidly form many Cu clusters in the system, heterogeneous nucleation of MnNiSi on the Cu clusters generally dominates, and the homogeneous nucleation of MnNiSi

phase is insignificant [36]. Mn, Ni and Si atoms slowly diffuse to the preexisting Cu clusters, forming a thin layer around the Cu and reducing the Cu/Fe interfacial energy. As the layer formed near the interface is just a few atomic layers at most, and since it is driven by reduction of the Fe/Cu interfacial energy, it is likely that the Mn, Ni and Si atoms are initially only weekly ordered or disordered, which is consistent with what is found from the LKMC model. Assuming a disordered MnNiSi layer, the X/MnNiSi (X = Fe, Cu) interfacial energies can be readily calculated within the framework of the nearest-neighbor broken-bond (NNBB) model [49] using the interactions in Table 1. The calculated interfacial energies are listed in Table 7.

Table 7 Interfacial energies for specific crystallographic orientations, estimated using the Nearest-Neighbor Broken-Bond model.

Interfacial energies for specific crystallographic orientations (mJ/m^2)	Cu-Fe	Cu-MnNiSi	Fe-MnNiSi
[100]	449	107	115
[110]	317	76	81
[111]	518	124	133

The interfacial energies estimated by the NNBB model show that a thin, disordered MnNiSi layer on the Cu/Fe interface reduces the total interfacial energy by ~50%. If the MnNiSi layer thickens as a disordered structure, the precipitate would grow in an isotropic manner around the Cu core, retaining a core-shell structure. However, as suggested by the LKMC simulation, the Mn, Ni and Si atoms instead form small ordered MnNiSi nuclei next to the Cu cluster. The precipitation process therefore can involve three distinct environments for a solute atom: dissolved in the matrix as a monomer, in the disordered coating layer, and in the ordered MnNiSi nuclei. The growth pathway of the precipitate depends on the relative energy of the solute atoms in the latter two states. For solute atoms, leaving the disordered coating layer will expose the Cu-Fe interface, thus increasing the total free energy of the system (the "interfacial energy contribution"). On the other hand, solute atoms leaving the disordered coating layer to join the ordered MnNiSi nuclei will also lower the total free energy of the system, due to the energy bonus from ordering (the "ordering energy contribution"). Comparing the two energy differences, if the former interfacial energy contribution is larger, exposing the Fe-Cu interface

will impose too high an energy penalty, in which case the coating layer would be stable. The stable coating layer would have time to rearrange locally to the ordered structure that is compatible to the growing front of the ordered nuclei. In this case, Cu cluster would eventually be fully covered by the MnNiSi phase, leading to the core-shell structure. If the latter ordering energy contribution is larger, it is energetically favorable for solute atoms to diffuse from the disordered coating layer to the ordered nuclei, either by surface diffusion or through the Cu core. As additional solute atoms diffuse from the matrix to the precipitate, atom transport from the coating layer to the ordered nuclei suppresses the symmetric thickening of the layer, leading to preferential growth of the ordered MnNiSi nuclei and results in the appendage morphology. We hypothesize that the ordering energy contribution dominates over the interfacial energy contribution, leading to the appendage structure.

To test our hypothesis, the LKMC simulation was rerun with an increased Cu-Fe interfacial energy, which was achieved by increasing the Cu-Fe interaction parameter $\Omega_{Cu\text{-}Fe}$ from 0.458eV to 0.758eV. In this case, the energetic penalty for MnNiSi atoms to leave the coating layer is significantly increased, and a more stable coating layer is expected. Figure 6(a) shows a snapshot of the simulated microstructure. Most of the Cu clusters are fully covered by the MnNiSi phase, forming the classic core-shell structure. In Figure 6(b), the distance between the COMs of the Cu cluster and the whole precipitate is plotted, together with the radius of the whole precipitate. It shows that as the whole precipitate grows in size, the magnitude of the distance between COMs does not increase, but fluctuates slightly above zero. This result confirms that during the growth process, the MnNiSi phase grows in an isotropic manner around the Cu cluster. The change in morphology from appendage to core-shell structures observed when the interfacial energy contribution is increased supports our hypothesis that the appendage structure occurs due to the larger size of the ordering vs. interfacial energy contributions.

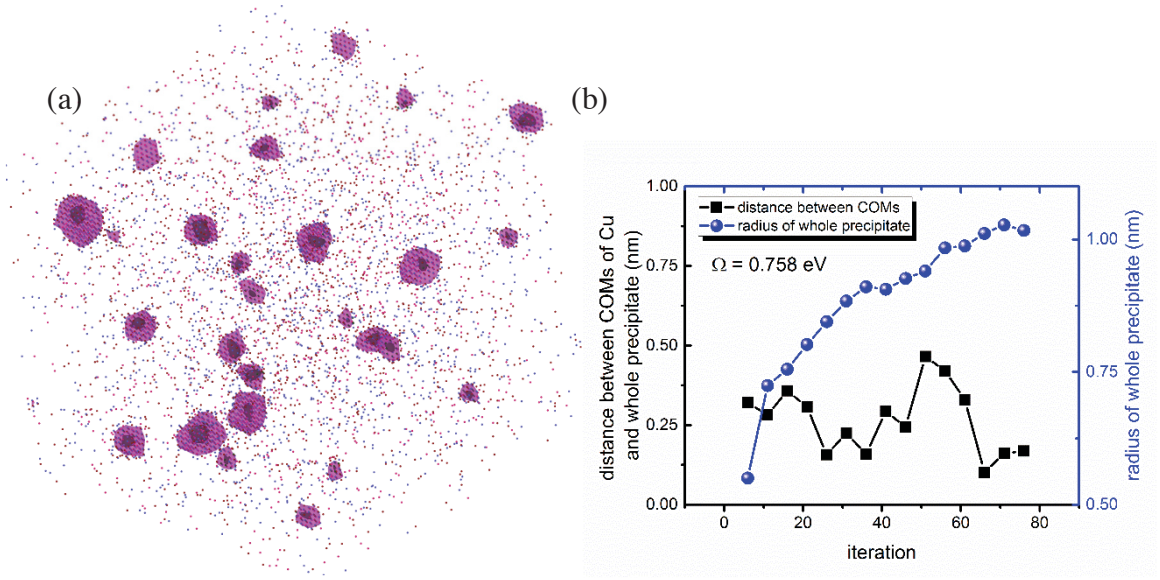

Figure 6 (a) Precipitate morphology for system with increased Cu-Fe interfacial enerngy (b) For the new set of parameters, distance between COMs as the precipitate grows, plotted for the largest precipitate in the system.

Another important observation is that, as shown in Figure 5(a), there is an absolute movement of the Cu cluster during growth. Given the fact that the lattice sites are conserved in the LKMC simulations, an absolute movement of Cu cluster toward one direction must be compensated by a net mass flux in the opposite direction, in this case, the flux of Mn, Ni and Si atoms. This observation suggests that during the process of the formation of Cu-MnNiSi precipitate, there is a diffusion path for Mn, Ni and Si atoms through the Cu clusters, i.e., the Cu clusters do not block the Mn, Ni and Si diffusion but serve as diffusion media, similar to the Fe matrix. This is an important point, since if the solute atoms would not diffuse through the Cu clusters, the Mn, Ni and Si build up and diffusion along the surface might easily cause the formation of the ordered MnNiSi phase at different locations along the surface, and potentially lead to Cu clusters being fully covered by the ordered MnNiSi phase, forming core-shell structures.

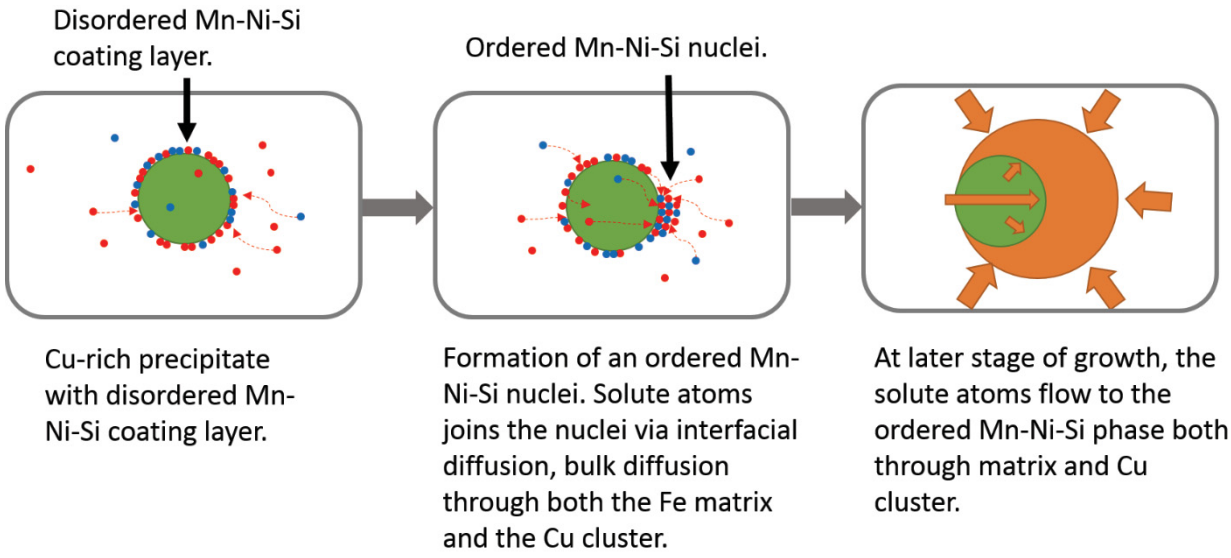

Figure 7 Schematics showing the kinetic pathway of the nucleation and growth of the Cu-MnNiSi co-precipitate. For interpretation of the references to color in this figure, the reader is referred to the web version of this article. Green: copper-rich precipitate; blue: Ni atom; red: Mn/Si atom; yellow: general representation of the Mn, Ni and Si solutes.

Based on the above discussion, we can summarize the proposed mechanism of the formation of the appendage morphology in Figure 7. For Cu solutes, their low solubility and fast kinetics lead to rapid formation of small Cu clusters. A disordered Mn-Ni-Si layer can readily form at the Cu/Fe interface to reduce the overall interfacial energy. This segregation of Mn, Ni and Si solutes at the Cu/Fe interface then leads to heterogeneous nucleation of the ordered nuclei of MnNiSi phase on one side of the Cu cluster. This ordered nuclei is more energetically favorable than nearby disordered Mn-Ni-Si and therefore grows via interfacial diffusion, as well as bulk diffusion through both the Fe matrix and the Cu cluster. In particular, the solute flux through the Cu cluster helps keep the Cu cluster at the edge of the whole precipitate during the process of the growth, supporting formation of the appendage morphology observed in both APT and LKMC.

4.2 Cluster Dynamics

4.2.1 Analysis of the large CD database on Mn-Ni-Si precipitates mole fraction

In the previous milestone we updated the cluster dynamics model by excluding the outlier experimental data at extreme conditions (very-low-solute-composition, very-high-flux and very-high-fluence) and provided a model that can predict the evolution of MNSPs in low-Cu RPV steels under both realistic power reactor and typical experimental high flux conditions. In this

milestone, we will model the combined effect on MNSPs mole fraction of a range of RPV alloy compositions, irradiation temperatures (T) and fluences (ϕt) presented as a series of cross plots of $\sqrt{f}$ versus a single variable, while holding the other variables constant. This analysis is focused on $\sqrt{f}$ *as* irradiation hardening ($\Delta\sigma_y$) and embrittlement (ΔT) primarily depend of the $\sqrt{f}$. These results were also included in the manuscript we recently submitted to Acta Materialia [50].

4.2.1.1 Alloy Composition and Fluence Effects

Figure 8 shows cross plots of the $\sqrt{f}$ versus Ni, over the specified range of Mn and Si at 10^{23}, $5\text{x}10^{23}$ and 10^{24} n·m^{-2} at 290°C and a flux of $3\text{x}10^{15}$n·m^{-2}s^{-1}. As mentioned previously, the $\sqrt{f}$ is used since it is the primary MNSP characteristic that controls $\Delta\sigma_y$ and ΔT.

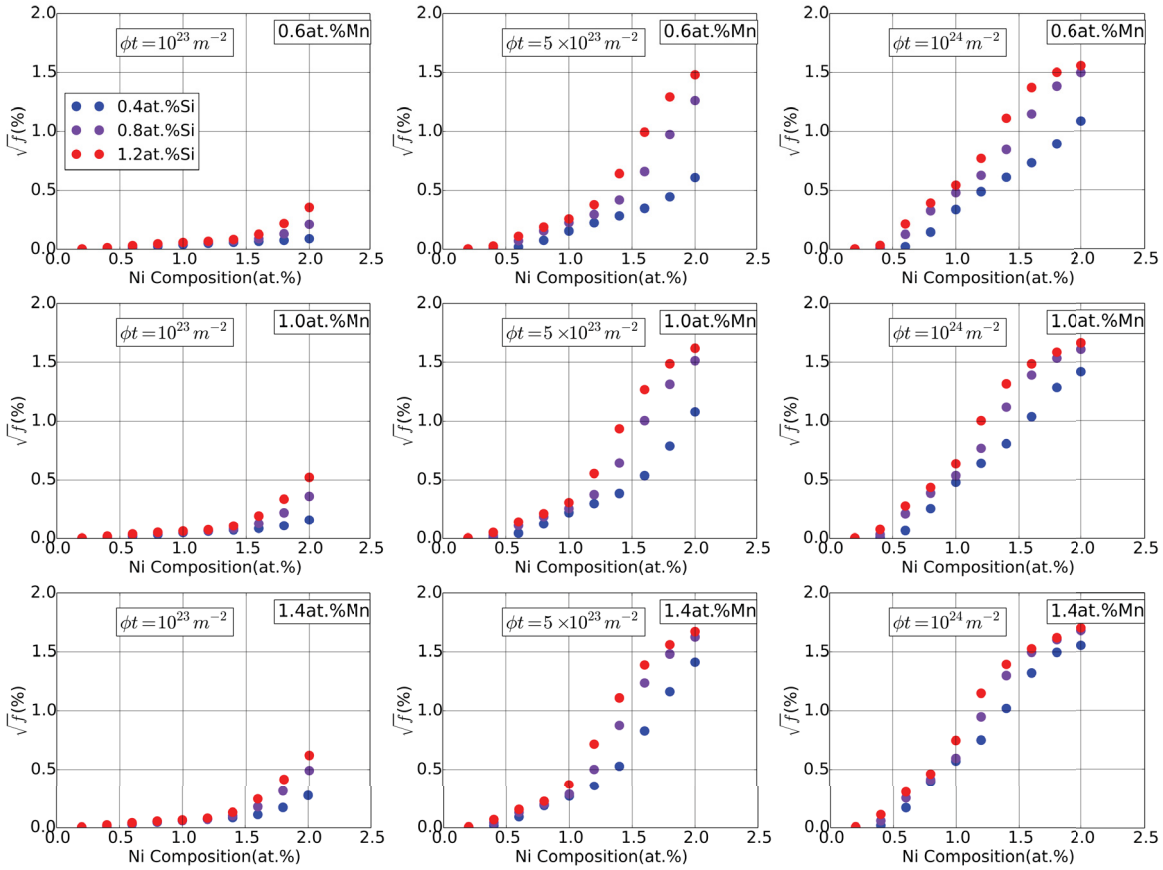

Figure 8 The square root of mole fraction ($\sqrt{f}$) as a function of Ni composition for various Mn and Si contents at different fluences.

Clearly Ni has a dominant effect on $\sqrt{f}$. The effects of Mn and Si are significant but more modest than they are for Ni. The absolute MNSP $\sqrt{f}$ is low at 10^{23} n·m^{-2}, but increases somewhat starting at ≈ 1.5at.%Ni. The effect of Ni is much stronger at $5\text{x}10^{23}$ n·m^{-2} above ≈ 0.5at.%Ni, and

$\sqrt{f}$ again increases rapidly above ≈ 1.5at.%Ni. At 10^{24} n·m^{-2} $\sqrt{f}$ increases approximately linearly, or with a weak polynomial dependence, between 0.5at.% and 1.6at.%Ni, and at higher Ni the increase in $\sqrt{f}$ begins to taper off.

We also developed a simple polynomial fit for $\sqrt{f}$ as a function of alloy composition at 10^{24} n·m^{-2} and 290°C, which can be used to estimate the mole fraction of precipitates without running CD models. For practical purposes the relevant ranges of bulk RPV steel compositions are ≈ 0.6-1.6at.%Ni, ≈ 0.4-1.2at.%Si and 0.6-2.0at.%Mn. However, the dissolved Mn is lower since this solute is also contained in carbides; further, most steels have less ≤ 1.6at.%Mn. Thus a practical range of dissolved Mn is ≈ 0.6-1.4at.%. Further, 1.0at.%Ni is the limit in the US surveillance database for low Cu steels. Here we focus on the peak extended life fluence of 10^{24} n·m^{-2}. Within this composition range, which is consistent with the formation of T3 (G) and T6 (Γ_2) phases, the $\sqrt{f}$ can be fit by a polynomial in the form

$$\sqrt{f} = C_0 + C_1 Ni + C_2 Ni^2, \tag{26}$$

Here the Cs are functions of (Mn + Si) where

C_0 = -2.58+2.8587(Mn+Si)-0.80652(Mn+Si)^2

C_1 =5.118-5.8233(Mn+Si)+1.6988(Mn+Si)^2

C_2 =-2.4783+3.2256(Mn+Si)-0.8823(Mn+Si)^2

Figure 9 compares the CD $\sqrt{f}$ to that predicted by Eq. (26). The agreement is excellent. This systematic behavior can be traced to fact that CD model predicts the formation of stoichiometric G and Γ_2 phases. The Γ_2 phase has almost 1 (Mn + Si) atom for every Ni atom. The G phase has ≈ 0.81(Mn + Si) atom for every Ni atom. Thus, while the overall effects of Mn and Si on the MNSP nucleation and growth at a specified temperature and fluence are more complex, to a first approximation they are associated with a varying balance of G and Γ_2 phases, that in both cases are reasonably represented by Eq. (26). Further, it has been experimentally observed that the effects of Mn and Si are individually relatively weak, due to the fact that their sum is typically approximately constant and roughly equal to the Ni in the MNSP. That is, if Si is low the MNSP is more enriched in Mn and vice versa. Note that non-stoichiometric phase-field effects are not captured in the current CD model, although the composition range of the phase-fields of both G and Γ_2 are quite small.

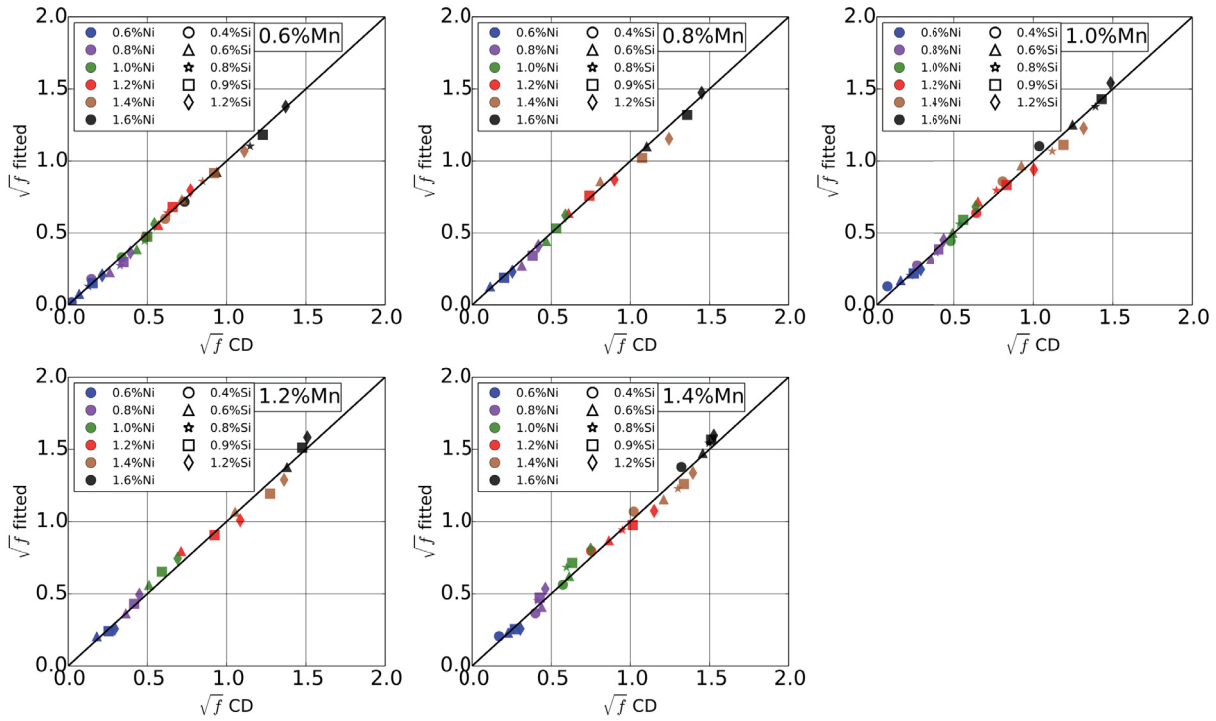

Figure 9 Comparison between fitted and results from CD for different alloy compositions

However, there is no simple relation between *f* and Ni for all combinations of composition. For example, low values of Mn or Si may be insufficient to form the *f* of G and Γ_2 phases that would otherwise be associated with very high Ni. Likewise, excess quantities of Mn and Si would remain in solution once the amounts of these solutes needed to form the modeled phases exceeded that required for a given Ni content.

Expressions similar to those in Eq. (26) can be derived from the CD database for other temperatures and fluences and compared to a wide variety of experimentally observed trends.

4.2.1.2 Temperature Effects

The MNSP *f* also depends strongly on the irradiation temperature (*T*). Figure 10 plots $\sqrt{f}$ versus *T* at Ni = 0.6at.%, 1.0at.%, 1.4at.% for 0.6at.%Si and 1.0at.%Mn at fluences of $5\text{x}10^{23}$ and $10\text{x}10^{23}$ $\text{n}\cdot\text{m}^{-2}$. Figure 10 a) shows that the absolute $\sqrt{f}$ increases with increasing Ni and decreasing *T*. Figure 10 b) shows the same data normalized to 1 at 290°C. In all cases the $\sqrt{f}$ versus *T* follows an approximately linear relation, and overall the trends are qualitatively similar.

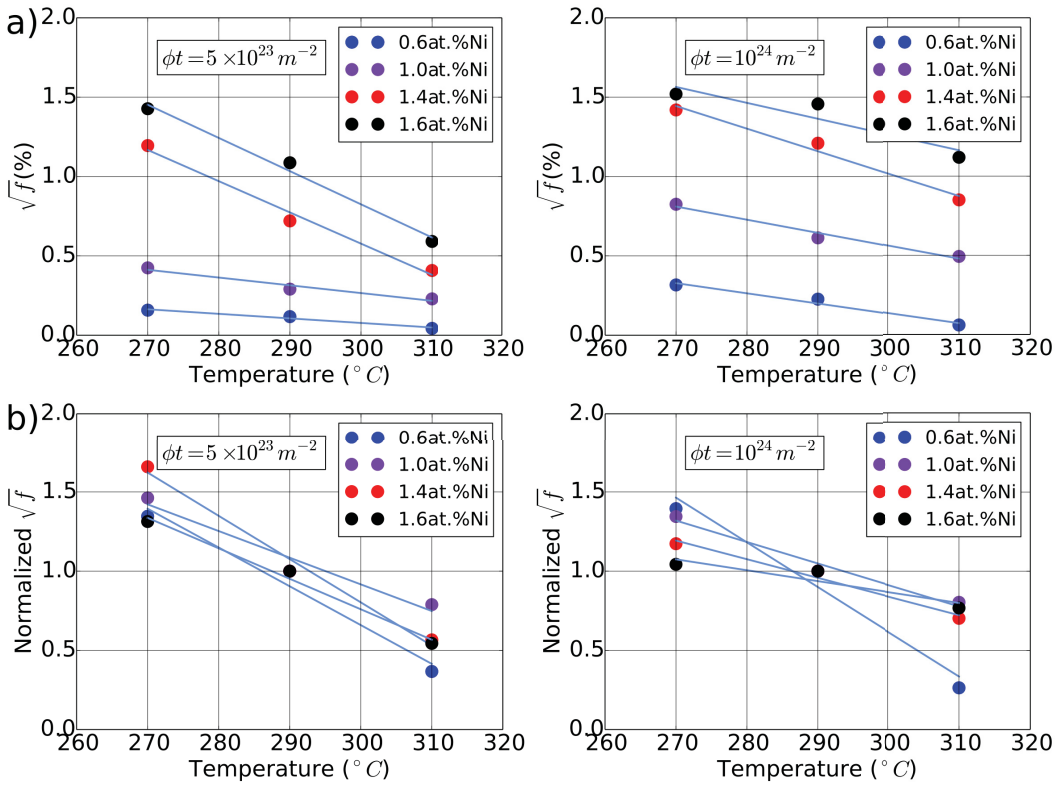

Figure 10 The effect of temperature on $\sqrt{f}$ for various alloy Ni contnets with 1.4at.%Mn-0.6%Si and two fluences: a) absolute √f; and, b) normalized to 1 at 290°C.

4.2.2 Precipitation in Cu bearing alloys

In this section, we parameterize the CD model proposed in section 3.2.3 for Cu+MnNiSi precipitates, and compare the modeling results with experimental data obtained from Odette group at UC-Santa Barbara. The experimental database contains full microstructural information (precipitates size, number density, and volume fraction) of 110 data points for four different alloys (LC, LD, LH, LI). Experiments are from IVAR, BR2-TU, and ATR1 irradiations and they cover a wide range of neutron flux (from 7×10^{14} to 2.3×10^{18} n/m^2/s) and temperature (270 to 320 °C). Microstructural measurement were done by using small angle neutron scattering (SANS) except for the highest fluence data from ATR1, which was done by atom probe measurement. Table 8 shows the alloys designation and their corresponding nominal composition.

Table 8. Alloys designation and corresponding nominal composition.

Alloy	Cu (at.%)	Ni (at.%)	Mn (at.%)	Si (at.%)
LC	0.36	0.81	1.46	0.46
LD	0.33	1.16	1.37	0.45

LH	0.09	0.69	1.38	0.43
LI	0.17	0.69	1.36	0.47

We note that the actual Cu and Mn remaining in solid solution that is available for radiation enhanced precipitation may be less than the measured bulk content, due to pre-precipitation during heat treatment performance during RPV fabrication. The maximum Cu and Mn remaining in solution after typical heat treatment is about 0.25 and 1.1 at.% respectively, and we therefore use these as the bulk composition limits in the modeling.

Based on the described methodology in section 3.2.3, in copper bearing alloys we have nucleation of both pure Cu and MNSPs. We note that the Cu content in all alloys listed in Table 8 is high enough to form Cu-rich precipitates. However, even if Cu is lower than 0.06at.% (the onset of Cu-rich precipitation formation in RPVs [27]), experimental results [51] suggest it can still enhance the nucleation of MNSPs. The effect of very low Cu (Cu<0.06at.%) on MNSP nucleation needs further investigation and has not yet been treated in detail in the model.

4.2.2.1 Parameters for Cu model

The precipitation of Cu in Fe was the subject of several modeling studies [52-58]. However, most of the previous models were for aging, and therefore they did not have the effect of irradiation on Cu precipitate evolution. Furthermore, previous models were generally compared to a limited set of experimental data points (e.g. aging at one single temperature for a fixed composition), which made them inapplicable across the many systems we are studying here. Therefore, we have developed our own model for Cu precipitation under irradiation. However, many necessary terms are available from previous models and we used these to guide the present model. Important parameters in modeling Cu precipitation are Cu solubility, diffusion coefficient, and interfacial energy. We obtain the Cu solubility from Soisson and Fu [58], which they determined by a combination of *ab initio* calculation and fitting to solubility data obtained from Fe-Cu aging at 550 and 450 °C [58]. We note that in RPV steels under irradiation the Cu precipitates sizes are smaller than 5-6 nm which is the onset of Cu structural transformation from BCC to R9 [59]. Therefore, it is important to use the Cu solubility when the equilibrium is between BCC Cu and Fe, as was determined in Ref. [58]. The solubility of Cu is modeled by the equation

$$C_{Cu}^{sol}(Fe) = \exp(\frac{\Delta S_{nc}}{k_B})\exp(-\frac{E_{Cu}^{sol}(Fe)}{k_B T}) \quad (27)$$

where ΔS_{nc} is the nonconfigurational entropy, $E_{Cu}^{sol}(Fe)$ is the formation energy (mixing energy) of a substitutional impurity Cu in Fe matrix, k_B is Boltzmann constant, and T is the temperature. Soisson and Fu [58] found the $E_{Cu}^{sol}(Fe) = 0.545\ eV$ based on *ab initio* calculations and $\Delta S_{nc} = 1k_B$ by fitting to experimental data.

Another important parameter is the Cu diffusion coefficient. The Cu diffusion coefficient in Fe has a wide range of values in the literature, as shown in Figure 11. Due to this uncertainty, we fit the Cu diffusion coefficient so that our model predictions match with the experimentally measured precipitation incubation fluence shown in Figure 12. The last key parameter is the Cu/Fe interfacial energy, which in general depends on the precipitate degree of coherency, crystallographic misorientation, elastic misfit strains, and solute segregation. Because of this complexity, interfacial energy generally cannot be determined reliably from direct experiment or atomistic calculations and it is usually treated as a fitting parameter in precipitation modeling. We fit the interfacial energy of Cu so that our model predictions give the minimum root mean square difference (RMSD) compared to experimental data for precipitate volume fraction, radius, and number density (shown in Figure 13). Note that the radiation enhanced diffusion necessary to model Cu precipitate evolution is treated exactly as for the rest of the CD model, as described in Sec. 3.2.1.3.

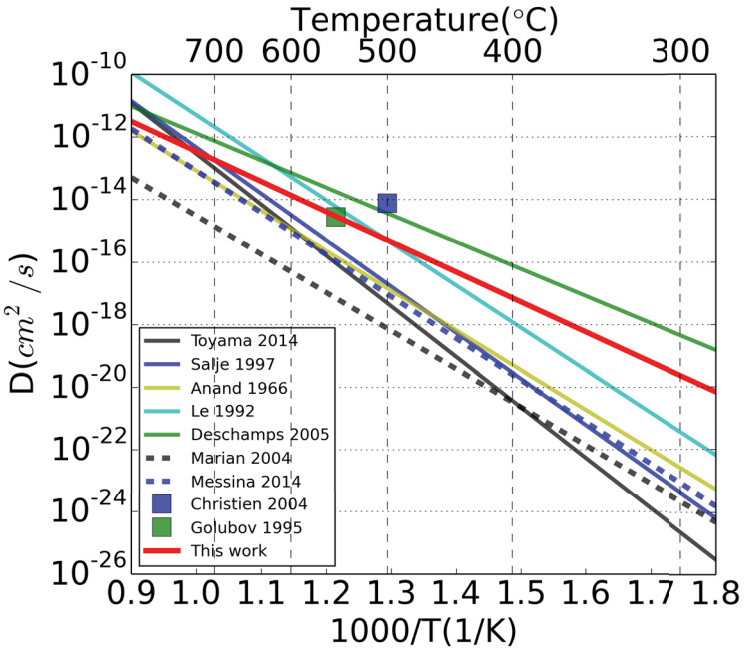

Figure 11. Cu diffusion coefficient in the literature [25, 60-67] and the fitted value in this work.

By using only homogeneous Cu nucleation, we were not able to get enough Cu precipitate nucleation to match the experiments. Specifically, for low Cu alloys like LI and LH which contain 0.17 and 0.09 at.% Cu, we do not see Cu precipitate formation in the fluence ranges for which it is seen experimentally. These inconsistencies indicate that Cu should also nucleate heterogeneously (similar to MNSPs). We note that the phenomenon of heterogeneous Cu nucleation in-cascade has already been reported by KMC modeling [68]. To incorporate the Cu in-cascade heterogeneous nucleation in CD, we use the similar formulation as we used for MNSPs (sections 3.2.1.2), except we modify the thermodynamic driving force to be that of Cu.

This approach yields the equation

$$R_{Cu-het}(n_{Cu-het},t) = \alpha_{Cu}.\sigma_{dpa}\phi/\Omega.K_{Cu}(t)/K_{Cu}^{0} \quad (28)$$

where α_{Cu} (n/cascade) is cascade cluster production efficiency factor, σ_{dpa} is the cross section of cascades, ϕ is irradiation flux, Ω is the atomic volume, $K_{Cu}(t)$ is the Cu concentration in matrix at time t, an K_{Cu}^{0} is the Cu solubility limit, which is equal to 3.6 x 10^{-5} at T = 290 °C. The other fitting parameter (rather than α) in heterogeneous Cu nucleation is the precipitate size that

is created during a cascade. Odette and Wirth's [68] KMC simulation showed that under irradiation Cu precipitates of size 5 to 20 atoms can form in cascades. Therefore, we fit the Cu precipitate size in the range of 5 to 20 atoms, again fitting to best match the data in Figure 12. Table 9 shows all the fitting parameters for the Cu part of CD model.

Table 9. Fitted parameters for Cu part of CD model

Parameter	**Value**
1. $D_{Cu}(m^2/s)$	$1.43\times10^{-7}\exp(-\frac{1.91}{k_BT})$
2. Interfacial energy (Cu-Fe) (J/m^2)	0.410
3. α $(\#/cascade)$	0.06
4. Heterogeneous Cu precipitate size (# of atoms)	12
5. The ratio of the number of atoms in MNSP to the number of atoms in Cu precipitate	0.4
6. Cu precipitate size above which create partner MNSP (# of atoms)	20 and larger

In summary, we fit the following parameters 1-6 in the Cu model (following the order of Table 9): (1) Cu Diffusion coefficient, (2) Cu-Fe interfacial energy, (3) number of nucleated Cu precipitates per cascade, (4) number of Cu atoms nucleated in each precipitate when nucleated in a cascade, (5) the ratio of MNSP to Cu in the partner MSNP growing with the Cu during Cu nucleation, (6) the size above which Cu precipitates create partner MNSP. Although we mentioned the fitting methods above, here we give a compact summary of the fitting order and data used in the fitting.

Independent of the other parameters we set the minimum number of atoms in Cu precipitates which create MNSPs (6) to be 20 atoms as that is close to Cu precipitates critical size. The results turn out to be quite insensitive to this value and we tested numbers between 10 to 100 and the results did not change significantly.

We fit the Cu diffusion coefficient (1) so that our model predictions match with the experimentally measured precipitation incubation fluence (the fluence before which significant precipitates appear) shown in Figure 12. This fit is done first with a reasonable guess for values for the parameters (2-5), and then redone again after parameters (2-5) were fit as below, although

it is not very sensitive to the values of parameters (2-5). The other remaining parameters (2-5) (interfacial energy (2), α (3), Cu precipitate heterogeneous size (4), and the ratio of MNSP size to Cu(5)) were then fit simultaneously in order to get minimum root mean squatter difference (RMSD) between model and experimental values for volume fraction, radius, and number density (data given in Figure 13). The optimization was done by minimizing an integrated cost function which contains a combination of root mean square deviation (RMSD) of the predictions from experimental results for mean radius, volume fraction, and number density, as was described in detail in a previous milestone from September 30, 2015.

The fitting ranges considered were as follows: for interfacial energy we explored 0.370 to 0.420 mJ/m^2 (0.4 is the value used in [27]) with mesh size of 0.01; for the cascade induced Cu precipitate size we explored the range of 5 to 20 atoms (based on KMC simulation in [68]) with an initial coarse mesh size of 5 atoms and then finer mesh of 2 atoms in range of 10 to 15 atoms; for α, the initial studies showed that α should be lower than 0.1. Therefore, we grid the 0-0.1 space with mesh of 0.03. For the ratio of MNSP size to Cu we first mesh the space of 0 to 1 with coarse mesh of 0.5 and then grid the promising domain with mesh of 0.1.

In Figure 12 we compare the CD model results and experimental data for evolution of precipitates in LC, LD, LH, and LI alloys as a function of fluence. In these plots, we run the CD code for an average environment condition (1x10^{16} n/m^2/s, 290 °C) to get a smooth average trend and run the CD code for all specific experimental data conditions to give the best possible comparison.

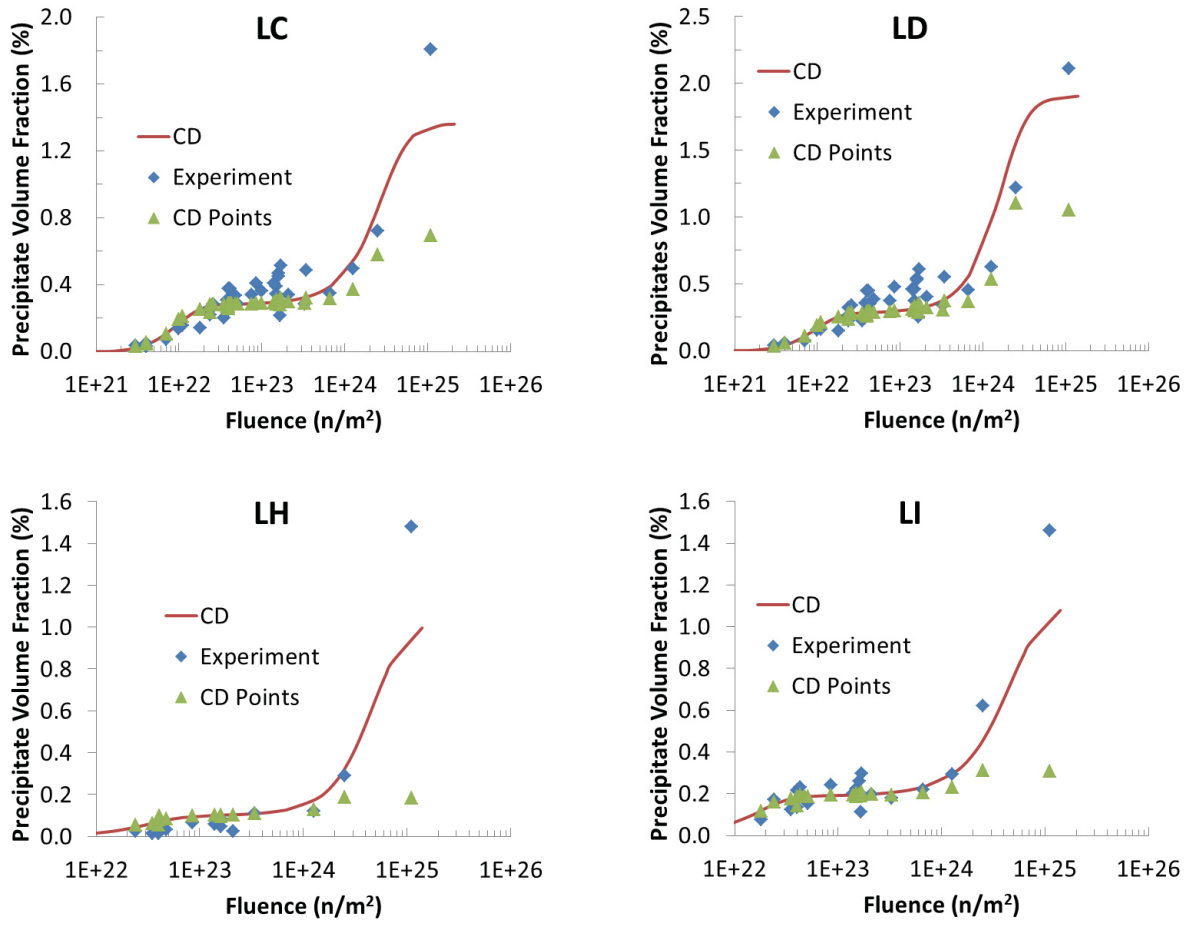

Figure 12. Comparison between CD model and experimental results for evolution of precipitates in LC, LD, LH, and LI alloys as a function of fluence. Red line is the CD results for an average irradiation condition ($1x10^{16}$ $n/m^2/s$, 290 °C). Green triangles denoted CD Points are values calculated at the exact conditions of the experiments.

We note that each experimental datum in Figure 12 has its own specific neutron flux (from $7x10^{14}$ to $2.3x10^{18}$ $n/m^2/s$) and temperature (from 270 to 320 °C) and these are the ones used in the CD model points labeled "CD Points". To compare the CD and experimental results more quantitatively, we plotted the CD predicted vs. actual values of precipitate radius, number density, and volume fraction in Figure 13.

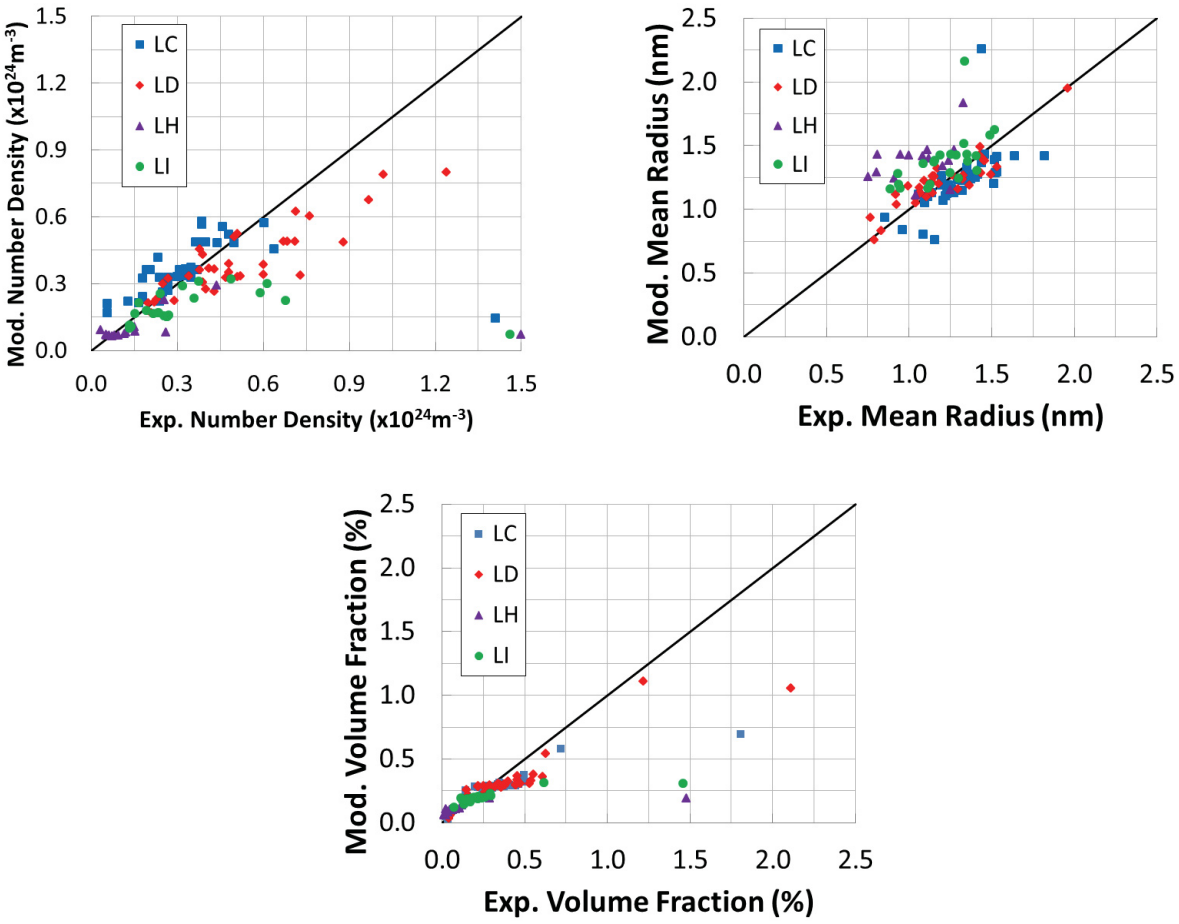

Figure 13. Comparison between CD and experimental results for precipitates number density, radius, and volume fraction.

From Figure 12 and Figure 13 we can see that, except for the highest fluence data point (which corresponds to ATR1 irradiations), the calculation results show a good agreement with the experimental results for a wide range of neutron flux (from $7x10^{14}$ to $2.3x10^{18}$ n/m^2/s), temperature (from 270 to 320 °C), fluence and composition. While we do not know exactly the cause of the CD predicted low number density (and consequently low volume fraction) for ATR1 data, we note that these data points have the highest neutron flux in data set, which could cause some radiation induced precipitation due to radiation induced segregation, which currently is not in the model. Similar problems were noted in the model predictions vs. other ATR1 data, as discussed in the previous report and in Sec. 4.2.1.

4.2.2.2 Model parameters validation

To further benchmark our Cu precipitation model for a different range of temperatures and compositions, we used the Cu parameters found for irradiated data to predict the Cu precipitation in Fe1.82at.%Cu0.2C1.38Al2.67Ni1.0Si0.5Mn under aging at 500 °C [69]. The comparison to these aging data is relevant as the alloy contains some amount of Mn, Ni, and Si, similar to the irradiated alloys being studied here. These elements can form a coating layer around Cu precipitates and mimic the similar morphology as we see in our KMC simulations and APT experiments of the RPV model alloys. Figure 14 shows the predicted Cu precipitates size and number density against experimental data [69]. The very good agreement between CD model (based on fitting parameters in Table 9) and experimental data strongly supports the validity of the Cu model. We also note that our model for Cu, which was fit to irradiation data on alloys with significant concentrations of other impurities, is only valid for other alloys with significant impurities. Tests for alloys without impurities (pure Fe-Cu) show significant discrepancies with our model predictions (Figure 15).

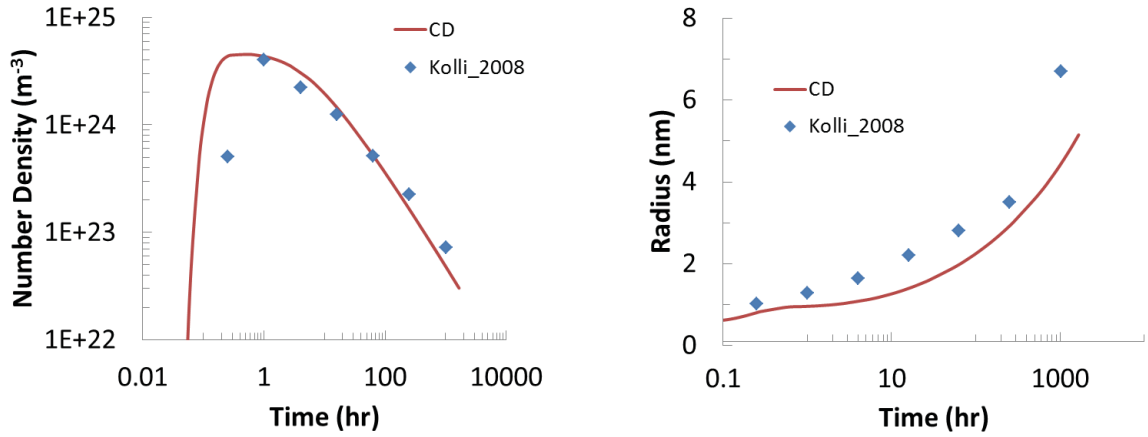

Figure 14. Comparison between CD model and experimental data [69] of Cu precipitation under aging at 500 °C. We note that the CD model parameters used here (Table 9) were obtained from fitting to irradiation data and not the data in this figure.

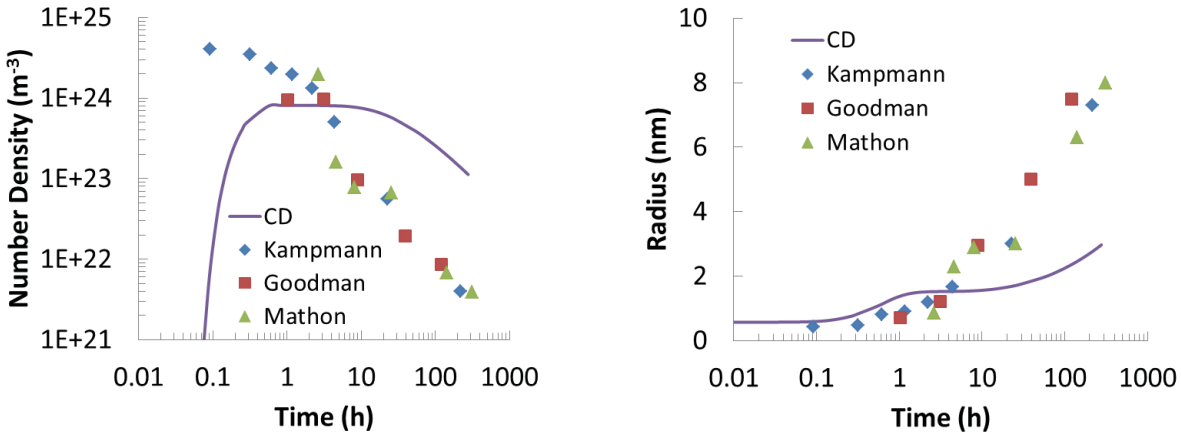

Figure 15. Comparison between CD model and experimental data [70-72] of Cu precipitation in pure Fe-1.34at.%Cu under aging at 500 °C. The CD parameters used here (Table 9) were obtained from fitting to irradiation data. Poor agreement between modeling and experimental data compared with good agreement in Figure 14 suggests the dramatic effects of other impurities (e.g. Mn, Ni, and Si) on the precipitation of Cu.

Another benchmark to show that the selected parameters (specifically interfacial energy) in Table 9 are in agreement with other experimental observations is to compare our prediction to experimental data on the minimum Cu for formation of Cu precipitates. The residual Cu in the RPV matrix is higher than equilibrium solubility limit due to excess free energy of precipitate-matrix interface, which is important for nanometer-size scales (the Gibbs Thompson effect). Based on test reactor data the minimum Cu threshold for forming Cu precipitates (these precipitates are likely decorated at the interface with other impurities, so we will refer to them as Cu-rich precipitates, or CRPs) is between ~ 0.05 and 0.08at.% Cu [33-35], and the EONY model uses 0.06at.% Cu as the minimum Cu for formation of CRPs [27]. In Figure 16 we plot the Cu fraction in the matrix verses fluence (flux=$1x10^{16}$ n/m^2/s and T= 290 °C) for different Cu levels (other elements are set at at.% 0.97Mn0.91Ni0.53Si). Figure 16 shows that for Cu lower than 0.06at.% the Cu fraction remains constant in the matrix, which indicate that no Cu precipitation forms for Cu lower than 0.06at.%, a result in good agreement with test reactor data and EONY model. Again, we note that this agreement is for alloys with significant concentrations of impurities that segregate to the Cu/Fe interface.

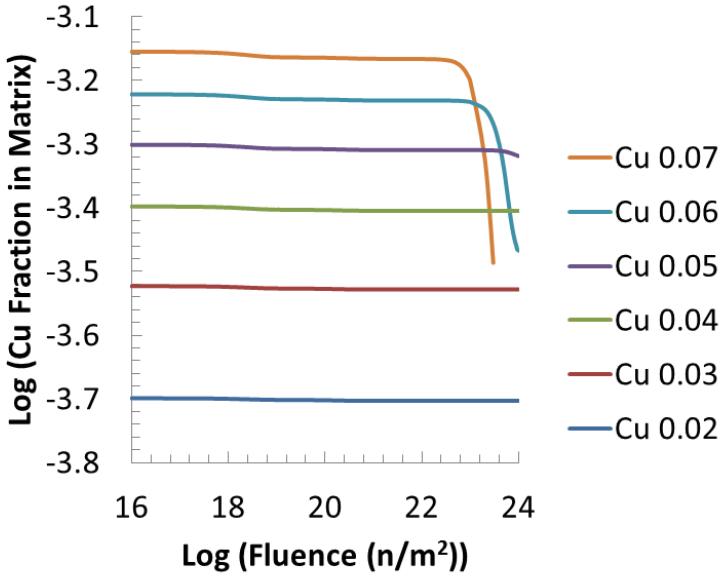

Figure 16. The minimum Cu (at.%) for formation CRP in RPV steels based on parameters in Table 9 (flux=1x10^{16} n/m^2/s , T= 290 °C, 0.9Mn0.9Ni0.25Si (at.%)).

4.2.2.3 Model predictability benchmark

We have recently received some new experimental data from the UCSB ATR2 irradiations from the Odette group at UCSB. These data are outside of the experimental database that we used to parameterize the model and we use these new data to check the accuracy of the CD model. The new ATR2 database include the full microstructural information of Cu-MNS precipitates (radius, number density, and volume fraction) of 28 atom probe tips from six different alloys (CM6, LC, LD, LG, LH, LI). These alloys were irradiated under the neutron flux of 3.64x10^{16} n/m^2/s at 291 °C up to the fluence of 1.39x10^{24} n/m^2. Figure 17 shows a very good agreement between CD predictions vs. experimental data. The statistical analysis shows that the RMSD for radius, number density, and volume fraction are 0.3 nm, 1.5x10^{23} m^{-3}, and 0.25 %, respectively. We note that the ATR2 experiment was done at fluence of 1.39 x10^{24} n/m^2 which is near the steep part of the volume fraction vs. fluence plot for many of these alloys (see Figure 12). Therefore, a small error in solutes diffusion under irradiation (which is likely due to the uncertainty in elements diffusion at ~290 °C and our simple RED model) could lead to a big error.

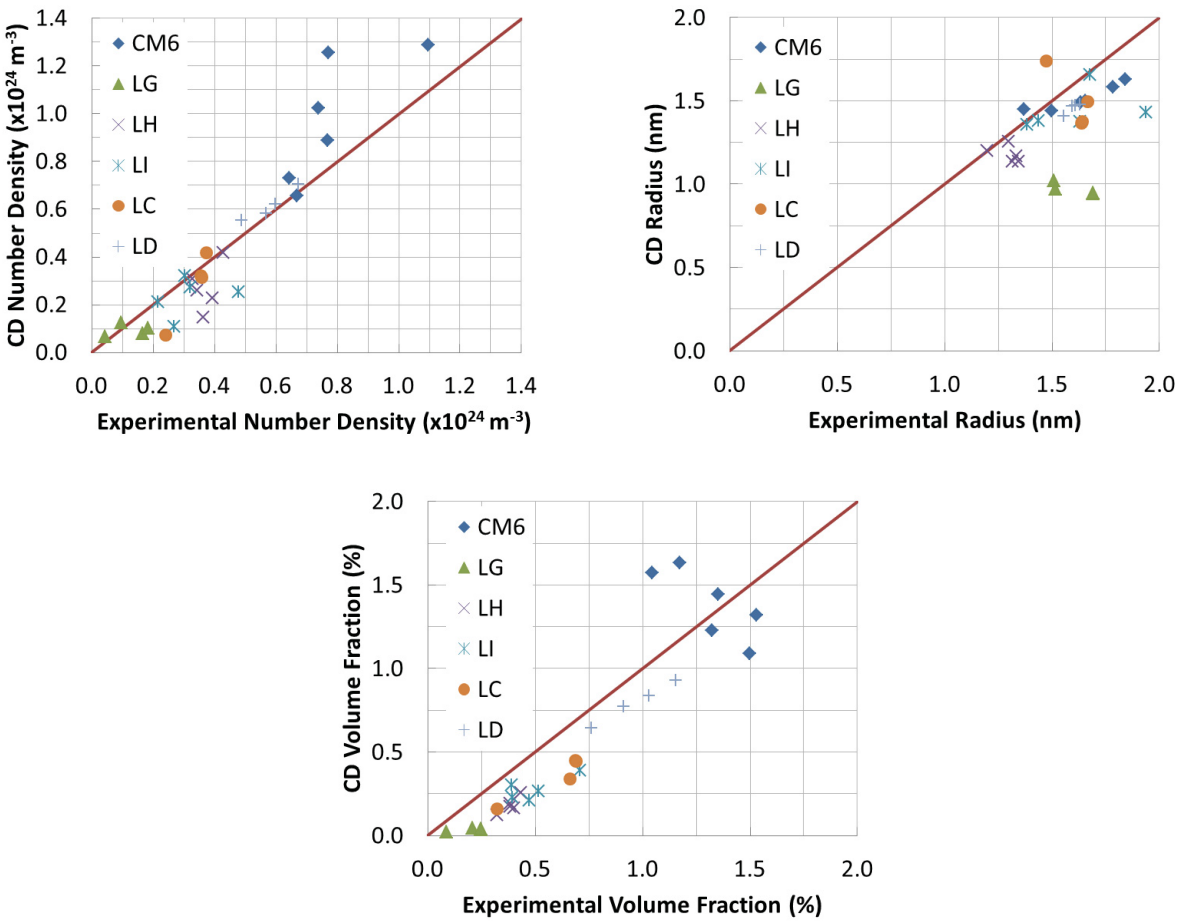

Figure 17. Comparison between CD and experimental results (from ATR2 tests) for precipitates number density, radius, and volume fraction.

One clear case where the CD model underestimated precipitation is for LG alloy, which has the lowest solutes among all the alloys considered. To study the effect of available solutes in alloys on CD accuracy we plotted the summation of all errors (error in radius, number density, and volume fraction) vs. total solutes in the alloys. Figure 18 clearly shows that the accuracy of CD model increase with solutes increase and we have higher error in low solute alloys. Reducing this error is the focus of future work.

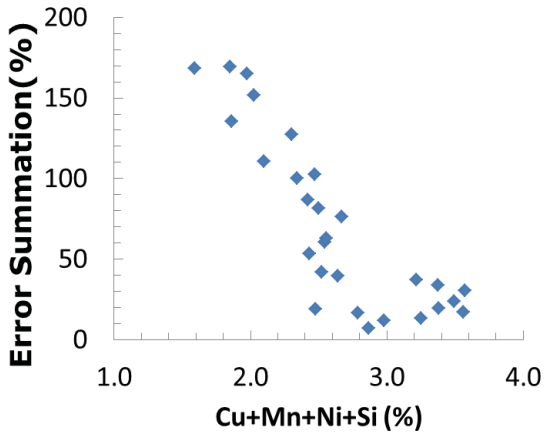

Figure 18. Correlation between available solutes in alloys and CD predictions error (sum of percent errors in number density, radius, and volume fraction) for ATR2 data. CD shows a higher error for low solute alloys.

4.2.2.4 Insights from the model

4.2.2.4.1 The effects of Cu on Cu-MNS precipitation in RPVs

As already discussed, Cu has very low solubility limit and high diffusion coefficient (compared with Mn, Ni, and Si) in Fe, which leads to very fast precipitation of supersaturated Cu. On the other hand, atomic interactions between solutes drag Mn-Ni-Si toward Cu precipitates. Therefore, Cu works as a catalyst in the formation of MNSPs. Figure 19 shows the predicted effect of Cu in formation of second phase precipitates for an alloy with medium solute content (1.0Mn1.0Ni0.4Si, at.%) under neutron flux of $1x10^{16}$ n/m^2/s at 290 °C.

Figure 19 shows the effect of Cu on Cu-MNS precipitation in RPVs. The main effect of Cu is on the number density of precipitates, where higher Cu makes the precipitation of Cu-MNS faster and more numerous. The volume fraction plot predicts that the presence of 0.3 at.% Cu can reduce the fluence required to initiate RPV embrittlement about two orders of magnitude.

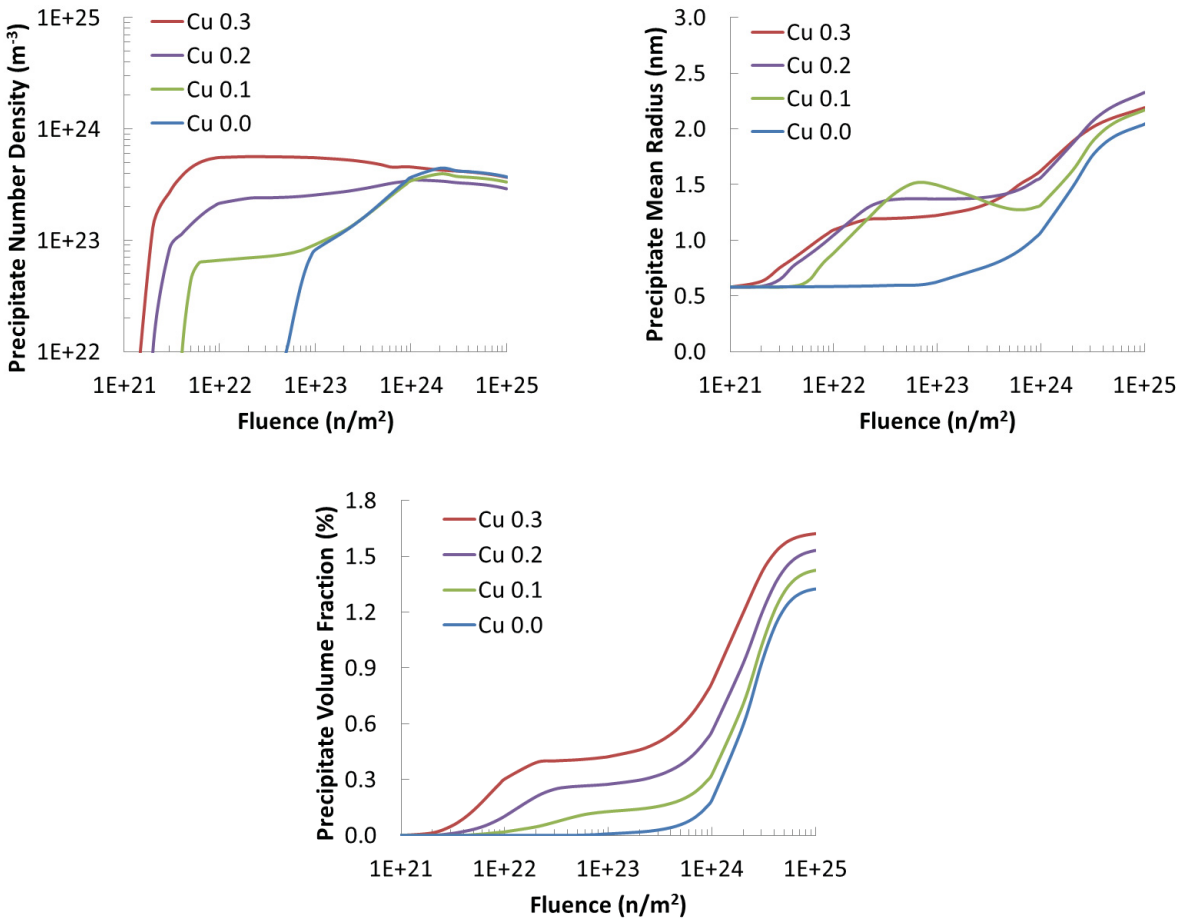

Figure 19. The effect of Cu on Cu-MNS precipitation in RPVs for a medium solute alloy (1.0Mn1.0Ni0.4Si, at.%.) under the flux of $1x10^{16}$ n/m^2/s at 290 °C.

4.2.2.4.2 LWR predictions

In Figure 20 we plot the evolution of precipitate volume fraction and DBTT for a low solute 0.7Mn0.85Ni0.25Si0.1Cu, medium solute 1.0Mn1.15Ni0.35Si0.2Cu, and high solute 1.3Mn1.75Ni0.65Si0.3Cu alloy under LWR conditions ($3x10^{14}$ n/m^2/s and 290 °C). We used the Russell-Brown model [73] to use the CD predictions of volume fraction and precipitate size to predict the yield stress shift, and then a simple linear scaling of temperature shift = 0.68×(yield stress shift)[36] to obtain the associated ductile to brittle transition temperature shift. One key result that we can get from Figure 20 is a qualitative understanding of the status of current RPVs in present reactors. The oldest operating reactor in the USA is less than 50 years old (Oyster Creek, Operating since 1969). Therefore, majority of current RPVs are still in the precipitation

growth regime, which indicates that the embrittlement data that we have from surveillance are lower than what the RPV steels will likely experience under life extension. This result also shows that most of the available Cu in the matrix precipitates out within the first couple of years of reactor operation and then the sluggish precipitation of MNS contribute over much longer periods to the RPV embrittlement.

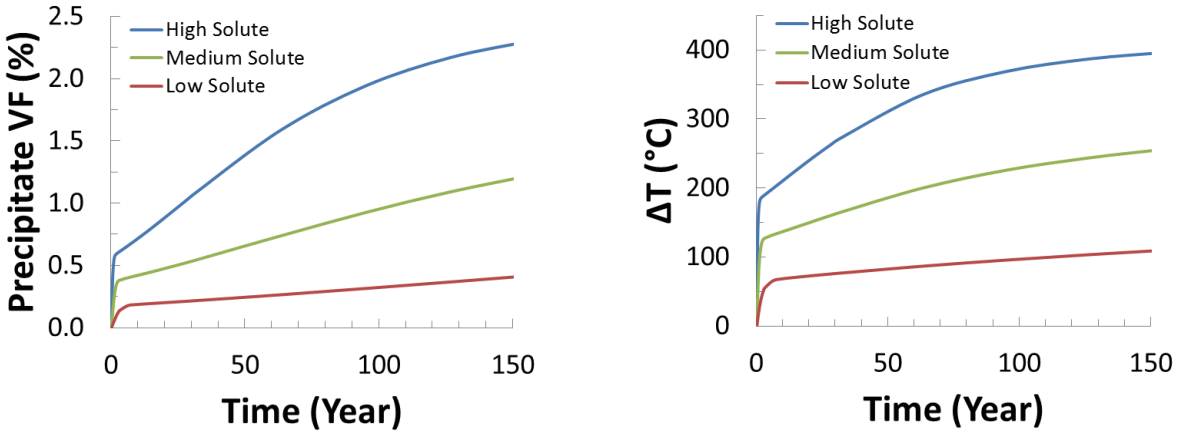

Figure 20. Precipitates volume fraction and ductile-to-brittle transition temperature as a function of time for low (0.7Mn0.85Ni0.25Si0.1Cu), medium (1.0Mn1.15Ni0.35Si0.2Cu), and high (1.3Mn1.75Ni0.65Si0.3Cu) solute alloys (all values at. %) under LWR conditions ($3x10^{14}$ $n/m^2/s$ and 290 °C).

4.3 Machine Learning

4.3.1 Results

Cross-validation (CV) assesses the predictive ability of the model and its independence from a particular training set. This section assesses the GKRR model using 5-fold CV and Leave-Out-Percent (LO X%) CV, and compares them to full fitting. For the 5-fold cross-validation, the dataset was split into five nominally equal parts, called folds. In a single test, the model was trained on the data in four of the five folds, then used to predict the left-out fold, with each fold being left out once. The RMSE for each test is given as the average RMSE over all five of the fold predictions. For the LO X% tests, in each test, the data was randomly split into a training set of (100-X)% of the data and a testing set of the remaining X% of the data.

Figure 21a shows a full fit RMSE of 17 MPa is for training the model on the complete set of IVAR+ experimental data and then predicting the data back according to the input. Figure 21b

shows results of best and worst fits for 5-fold CV, and also shows the 5-fold CV RMSE of 20.5 +/- 0.3 MPa averaged over 200 tests. The similarity in fully fitted RMSE and CV RMSE shows that the model is not prone to over-fitting. These encouraging results show that the model is robust for predicting back IVAR+ data. Future work will involve attempting to predict LWR-condition data.

a)

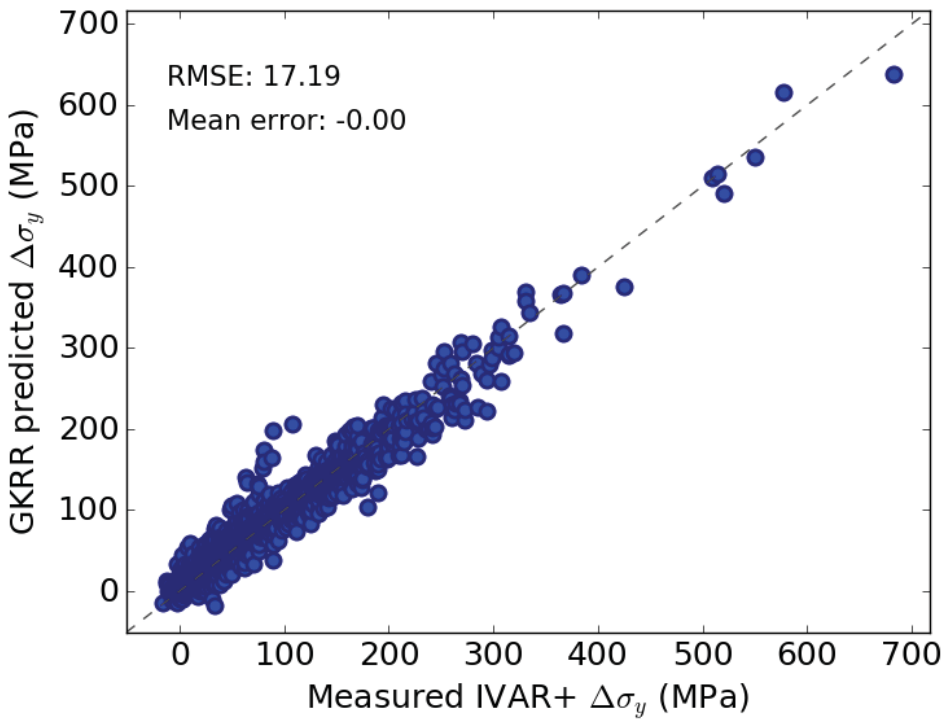

b)

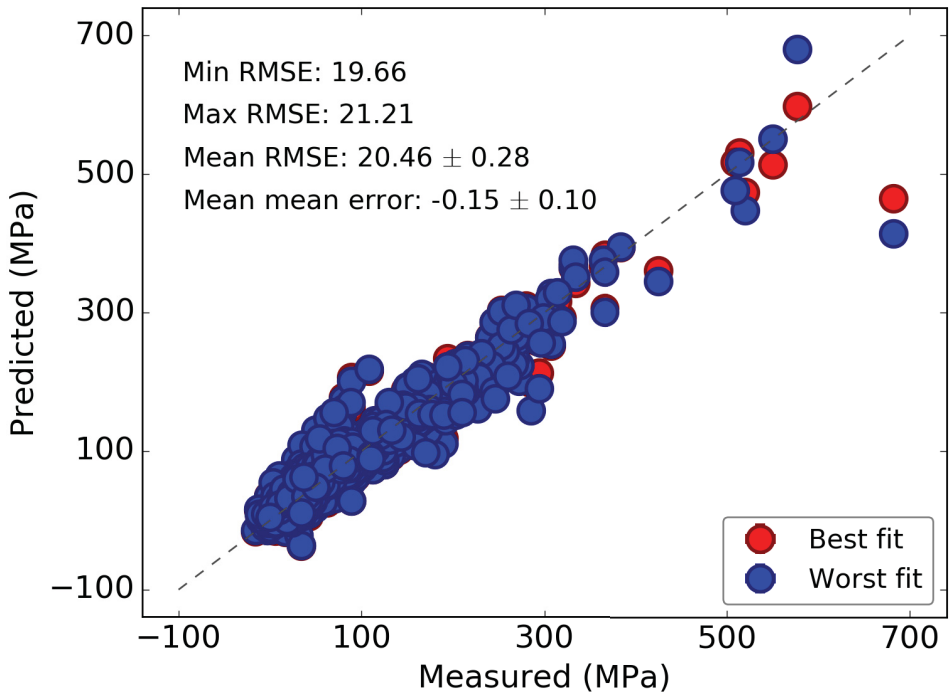

Figure 21. (a) Full fitting and (b) 5-fold cross-validation of IVAR+ experimental data using the GKRR model. The best and worst CV fits are evaluated out of 200 cross-validation tests. For each cross-validation test, the RMSE values from each of the five folds are averaged into a single RMSE value. The best CV fit has the lowest fold-average RMSE of the 200 tests, and the worst CV fit has the highest fold-average RMSE. The points shown in red or blue are for all five folds of each test.

4.3.2 Additional cross validation

Figure 22 shows the results of Leave Out (LO) percentage tests, where a fixed percentage of the data is randomly selected to be removed from the training set, and that data then becomes the testing set. Naturally, LO20% performs better than LO50% and LO80%, as more data is trained upon. However, the worst fits for LO50% and LO80% generally involve only a few outliers, and even so the RMSE is lower than 50 MPa.

Figure 23 shows the results of leave-one-out (LOO) cross validation, which has an RMSE and appearance comparable to full fitting and 5-fold cross validation.

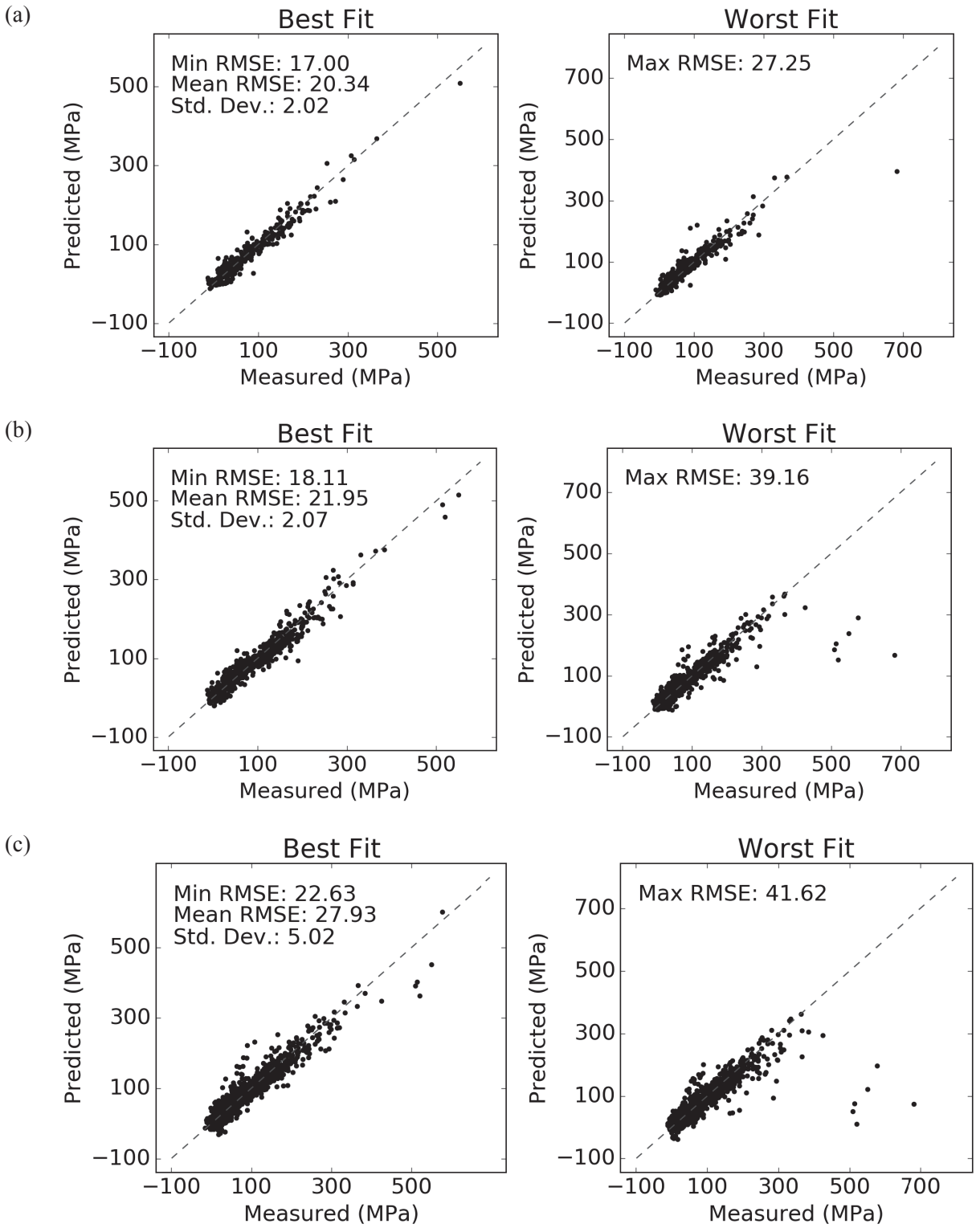

Figure 22. Best (lowest RMSE) and worst (highest RMSE) test predictions out of 200 CV tests where (a) 20%, (b) 50%, and (c) 80% of the data was selected by random to be left out of the training set.

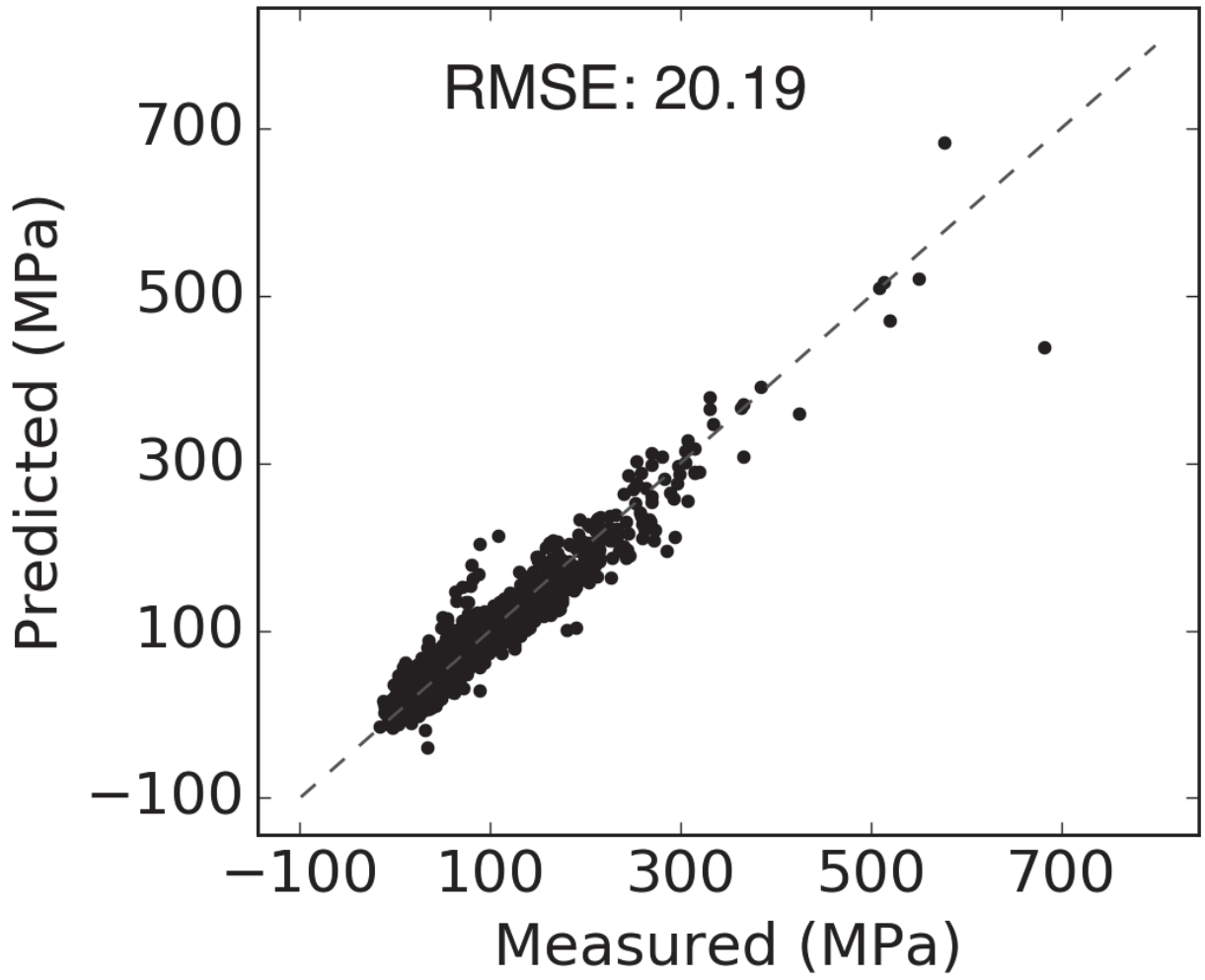

Figure 23. Measured and predicted values for leave-one-out CV.

5. SUMMARY OF MAJOR RESULTS

5.1 Kinetic Monte Carlo (KMC)

- KMC simulations were used to reproduce the formation of the Cu-MnNiSi appendage microstructure during co-precipitation. The KMC models provided insights on Cu+Mn-Ni-Si precipitates (MNSPs) growth to help model their coupled evolution with cluster dynamics.
- Detailed analysis indicates that the ordered MNS nuclei on the Cu/Fe interface provide a lower energy state compared to the disordered MNS coating layer on the Cu-rich precipitate, leading to unstable coating layer and preferential growth of the ordered phase on one side of the Cu core.
- In addition, there exists a diffusion path for MnNiSi atoms through the Cu core, pushing the Cu core to the edge of the Cu-MnNiSi precipitate and creating Cu-core-MnNiSi-appendage structure.

5.2 Cluster Dynamics

5.2.1 Cu-free alloys

- The alloy Ni content is the dominant compositional factor in forming MNSPs, while Mn and Si play lesser roles. The dominant role of Ni is due to the fact the G and Γ_2 phases respectively contain 1 and 0.8 (Mn + Si) atoms for every Ni atom, respectively.
- The absolute threshold for MNSPs formation appears to be ≈ 0.5at.%Ni.
- The $\sqrt{f}$ of MNSPs at extended RPV life fluence of $10^{24}m^{-2}$ at 290°C can be fitted to a polynomial of alloy compositions, which can be used for quick estimation.
- The $\sqrt{f}$ versus T follows an approximately linear relation

5.2.2 Cu bearing alloys

- Even a small amount of Cu (e.g. 0.09at.%) can dramatically enhance the speed of RPV steel embrittlement by catalyzing the formation of MNSPs.
- The predictive accuracy of the CD model was benchmarked against ATR2 experimental data and fairly good agreement was obtained, although percentage errors increase significantly as solute fraction is reduced.

- The main effect of increasing Cu on MnNiSi precipitates is to initiate their more rapid nucleation and increase the precipitates number density.
- For LWR conditions ($3x10^{14}$ $n/m^2/s$ and 290 °C), unlike Cu-free RPV steels, where the major embrittlement starts around 50 years of operation (for medium solute containing alloys, i.e. 1.0at.%Mn1.0Ni0.4Si), Cu bearing alloys (Cu>0.1at.%) experience embrittlement from very beginning of operation due to rapid Cu precipitate over less than one year and then accelerated MnNiSi precipitation.

5.3 Machine Learning

- Machine learning using Gaussian Kernel Ridge Regression (GKRR) predicts the change in yield stress for compositions and conditions represented within the IVAR/IVAR+ database with an RMSE of 17 MPa for a full fit.
- Cross validation RMSE for 5-fold and leave out 20% data average approximately 20 MPa. The similar full-fit and cross validation RMSEs suggest little over-fitting.
- This model will now be explored for its capabilities in predicting LWR condition hardening.

6. FUTURE WORK

The main focus of additional work is in improving the CD and machine learning models. The main focus of additional CD work will be extending the Cu+MNSP model to lower Cu-bearing alloy (lower than 0.06at.% when the CRP will not form), identifying and fixing the source of errors in low-solute and intermediate Ni alloys, identifying and fixing the source of errors in very high flux ATR1 condition simulations, enhancing the model beyond simple p-scaling for treating radiation enhanced diffusion, and refining the model by fitting to both all the available microstructural data and to the IVAR hardening database through empirical mechanical property models. The machine learning models will be tested and improved by using virtual data of hardening vs. flux, fluence, temperature and composition that include both measured conditions, e.g., like those in IVAR, and unmeasured LWR conditions. These virtual data sets will be generated by models like our CD model and can be used to test the predictive ability of the machine learning approaches. Additional work beyond the CD and machine learning models is focused on exploring new atom probe experiments on Cu precipitation to better understand flux and alloying effects in a pair of simple model alloys.

References

1. Enrique, R.A. and P. Bellon, *Compositional patterning in immiscible alloys driven by irradiation.* Physical Review B, 2001. **63**(13).
2. Shu, S., P. Bellon, and R.S. Averback, *Role of point-defect sinks on irradiation-induced compositional patterning in model binary alloys.* Physical Review B, 2015. **91**(21): p. 214107.
3. Doyama, M. and J.S. Koehler, *The relation between the formation energy of a vacancy and the nearest neighbor interactions in pure metals and liquid metals.* Acta Metallurgica, 1976. **24**(9): p. 871-879.
4. Messina, L., et al., *Exact ab initio transport coefficients in bcc Fe-X (X=Cr, Cu, Mn, Ni, P, Si) dilute alloys.* Physical Review B, 2014. **90**(10): p. 104203.
5. Martin, G. and P. Bellon, *Driven alloys*, in *Solid State Physics - Advances in Research and Applications, Vol 50*, H. Ehrenreich and F. Spaepen, Editors. 1997, Elsevier Academic Press Inc: San Diego. p. 189-331.
6. Nastar, M. and F. Soisson, *Atomistic modeling of phase transformations: Point-defect concentrations and the time-scale problem.* Physical Review B, 2012. **86**(22).
7. Odette, G.R., T. Yamamoto, and D. Klingensmith, *On the effect of dose rate on irradiation hardening of RPV steels.* Philosophical Magazine, 2005. **85**(4-7): p. 779-797.
8. Liu, C.L., et al., *A lattice Monte Carlo simulation of nanophase compositions and structures in irradiated pressure vessel Fe-Cu-Ni-Mn-Si steels.* Materials Science and Engineering: A, 1997. **238**(1): p. 202-209.
9. Vincent, E., C.S. Becquart, and C. Domain, *Microstructural evolution under high flux irradiation of dilute Fe–CuNiMnSi alloys studied by an atomic kinetic Monte Carlo model accounting for both vacancies and self interstitials.* Journal of Nuclear Materials, 2008. **382**(2–3): p. 154-159.
10. Schmelzer, J., *A new approach to nucleation theory and its application to phase formation processes in glass-forming melts.* Physics and chemistry of glasses, 2004. **45**(2): p. 116-120.
11. Schmelzer, J.W., A.S. Abyzov, and J. Möller, *Nucleation versus spinodal decomposition in phase formation processes in multicomponent solutions.* The Journal of chemical physics, 2004. **121**(14): p. 6900-6917.
12. Schmelzer, J.W., A.R. Gokhman, and V.M. Fokin, *Dynamics of first-order phase transitions in multicomponent systems: a new theoretical approach.* Journal of colloid and interface science, 2004. **272**(1): p. 109-133.
13. Slezov, V.V., *Kinetics of first-order phase transitions*. 2009: John Wiley & Sons.
14. Liu, C., et al., *A lattice Monte Carlo simulation of nanophase compositions and structures in irradiated pressure vessel Fe-Cu-Ni-Mn-Si steels.* Materials Science and Engineering: A, 1997. **238**(1): p. 202-209.
15. Wells, P. and G.R. Odette, *Atom probe tomography study of CuMnNiSi precipitation in reactor pressure vessel,* . Private Communication 2016.
16. Zhang, Y., et al., *Preferential Cu precipitation at extended defects in bcc Fe: An atomistic study.* Computational Materials Science, 2015. **101**: p. 181-188.
17. Cahn, J.W., *Nucleation on dislocations.* Acta Metallurgica, 1957. **5**(3): p. 169-172.
18. Dudarev, S.L., R. Bullough, and P.M. Derlet, *Effect of the alpha-gamma phase transition on the stability of dislocation loops in bcc iron.* Physical Review Letters, 2008. **100**(13).
19. Eason, E.D., et al., *A Physically Based Correlation of Irradiation-Induced Transition Temperature Shifts for RPV Steels.* ORNL/TM-2006/530 2007.
20. Zhang, X., et al., *Precipitate stability in Cu–Ag–W system under high-temperature irradiation.* Acta Materialia, 2015. **97**(0): p. 348-356.

21. Nohara, K. and K. Hirano. *Diffusion of Mn(54) in iron and iron-manganese alloys*. in *International Conference on Science and Technology of Iron and Steels*. 1971. The Iron and Steel Institute of Japan.
22. Hirano, K., M. Cohen, and B.L. Averbach, *Diffusion of nickel into iron.* Acta Materialia, 1961. **9**(5): p. 440-445.
23. Borg, R.J., *Diffusion in α-Fe-Si Alloys.* Journal of Applied Physics, 1970. **41**(13): p. 5193.
24. James, D.W. and G.M. Leak, *Self-diffusion and diffusion of cobalt in alpha and delta-iron.* Philosophical Magazine, 1966. **14**(130): p. 701-713.
25. Christien, F. and A. Barbu, *Modelling of copper precipitation in iron during thermal aging and irradiation.* Journal of Nuclear Materials, 2004. **324**(2-3): p. 90-96.
26. Odette, G.R., Private Communication, 2015.
27. Odette, G., R. Nanstad, and T. Yamamoto, *A physically based correlation of irradiation-induced transition temperature shifts for RPV steels.* 2007.
28. Wells, P., et al., *Atom probe studies of the nano-scale Mn-Ni-Si precipitates for RPV steels under irradiation.* Accepted by Acta Materialia, 2014.
29. Miller, M.K., et al., *APT characterization of high nickel RPV steels.* Journal of Nuclear Materials, 2006. **351**(1-3): p. 187-196.
30. Miller, M.K., et al., *APT characterization of irradiated high nickel RPV steels.* Journal of Nuclear Materials, 2007. **361**(2-3): p. 248-261.
31. Miller, M.K. and K.F. Russell, *Embrittlement of RPV steels: An atom probe tomography perspective.* Journal of Nuclear Materials, 2007. **371**(1–3): p. 145-160.
32. Fujii, K., et al., *Hardening and microstructural evolution in A533B steels under high-dose electron irradiation.* Journal of Nuclear Materials, 2005. **340**(2-3): p. 247-258.
33. Odette, G., T. Yamamoto, and D. Klingensmith, *On the effect of dose rate on irradiation hardening of RPV steels.* Philosophical Magazine, 2005. **85**(4-7): p. 779-797.
34. Odette, G. and G. Lucas, *Recent progress in understanding reactor pressure vessel steel embrittlement.* Radiation effects and defects in solids, 1998. **144**(1-4): p. 189-231.
35. Odette, G., et al., *Multiscale-multiphysics modeling of radiation-damaged materials: embrittlement of pressure-vessel steels.* Mrs Bulletin, 2001. **26**(03): p. 176-181.
36. Wells, P.B., et al., *Evolution of manganese–nickel–silicon-dominated phases in highly irradiated reactor pressure vessel steels.* Acta Materialia, 2014. **80**: p. 205-219.
37. Odette, G.R. *Modeling of Irradiation Embrittlement in Pressure Vessel Steels*. in *Irradiation Effects on Pressure Vessel Steels*. 1998. Vienna, Austria: IAEA IRRWG-LMNPP98-3, International Atomic Energy Agency.
38. Castin, N., L. Malerba, and R. Chaouadi, *Prediction of radiation induced hardening of reactor pressure vessel steels using artificial neural networks.* Journal of Nuclear Materials, 2011. **408**: p. 30-39.
39. Kemp, R., et al., *Neural-network analysis of irradiation hardening in low-activation steels.* Journal of Nuclear Materials, 2006. **348**: p. 311-328.
40. Eason, E.D., et al., *A physically-based correlation of irradiation-induced transition temperature shifts for RPV steels.* Journal of Nuclear Materials, 2013. **433**(1–3): p. 240-254.
41. *Python*. 2014; Available from: https://www.python.org
42. Pedregosa, F., et al., *Scikit-learn: Machine Learning in Python.* Journal of Machine Learning Research, 2011. **12**: p. 2825-2830.
43. Wagner, A., et al., *Effect of neutron flux on the characteristics of irradiation-induced nanofeatures and hardening in pressure vessel steels.* Acta Materialia, 2016. **104**: p. 131-142.
44. Styman, P.D., et al., *Precipitation in long term thermally aged high copper, high nickel model RPV steel welds.* Progress in Nuclear Energy, 2012. **57**: p. 86-92.
45. Hyde, J.M., et al., *A comparison of the structure of solute clusters formed during thermal ageing and irradiation.* Ultramicroscopy, 2011. **111**(6): p. 664-671.

46. Wells, P., et al., *On the Thermal Stability of Features Formed in Highly Irradiated Reactor Pressure Vessel Steels*. (in preparation).
47. Sprouster, D.J., et al., *Structural characterization of nanoscale intermetallic precipitates in highly neutron irradiated reactor pressure vessel steels.* Scripta Materialia, 2016. **113**: p. 18-22.
48. Zhang, C. and M. Enomoto, *Study of the influence of alloying elements on Cu precipitation in steel by non-classical nucleation theory.* Acta Materialia, 2006. **54**(16): p. 4183-4191.
49. Sonderegger, B. and E. Kozeschnik, *Generalized Nearest-Neighbor Broken-Bond Analysis of Randomly Oriented Coherent Interfaces in Multicomponent Fcc and Bcc Structures.* Metallurgical and Materials Transactions a-Physical Metallurgy and Materials Science, 2009. **40A**(3): p. 499-510.
50. Ke, H., et al., *Cluster dynamics modeling of Mn-Ni-Si precipitates in low-Cu reactor pressure vessel steels*. submitted to Acta Materialia.
51. Radiguet, B., et al. *Effect a Cu level on the microstructure evolution of 16MND5 steels from EDF surveillance program*. in *IGRDM 16*. 2011. Santa Barbara, USA.
52. Barashev, A., et al., *Copper precipitation in Fe–Cu alloys under electron and neutron irradiation.* Acta materialia, 2004. **52**(4): p. 877-886.
53. Castin, N., M.I. Pascuet, and L. Malerba, *Modeling the first stages of Cu precipitation in α-Fe using a hybrid atomistic kinetic Monte Carlo approach.* The Journal of chemical physics, 2011. **135**(6): p. 064502.
54. Christien, F. and A. Barbu, *Modelling of copper precipitation in iron during thermal aging and irradiation.* Journal of nuclear materials, 2004. **324**(2): p. 90-96.
55. Gokhman, A., J. Boehmert, and A. Ulbricht, *Kinetic study of copper precipitates under VVER-type reactor conditions.* Radiation effects and defects in solids, 2003. **158**(11-12): p. 783-792.
56. Golubov, S., et al., *The evolution of copper precipitates in binary Fe Cu alloys during ageing and irradiation.* Journal of nuclear materials, 1995. **226**(1): p. 252-255.
57. Jourdan, T., et al., *Influence of cluster mobility on Cu precipitation in α-Fe: A cluster dynamics modeling.* Acta Materialia, 2010. **58**(9): p. 3400-3405.
58. Soisson, F. and C.-C. Fu, *Cu-precipitation kinetics in α− fe from atomistic simulations: Vacancy-trapping effects and cu-cluster mobility.* Physical Review B, 2007. **76**(21): p. 214102.
59. Heo, Y.-U., et al., *Phase transformation of Cu precipitates from bcc to fcc in Fe–3Si–2Cu alloy.* Acta Materialia, 2013. **61**(2): p. 519-528.
60. Salje, G. and M. Feller-Kniepmeier, *The diffusion and solubility of copper in iron.* Journal of Applied Physics, 1977. **48**(5): p. 1833.
61. Anand, M.S., *Diffusion of Copper in Iron.* Journal of Applied Physics, 1966. **37**(11): p. 4248.
62. Marian, J., et al., *Cu diffusion in α-Fe: determination of solute diffusivities using atomic-scale simulations.* Computational Materials Science, 2004. **31**: p. 347-367.
63. Golubov, S., et al., *The evolution of copper precipitates in binary Fe-Cu alloys during ageing and irradiation.* Journal of nuclear materials, 1995. **226**: p. 252-255.
64. Toyama, T., et al., *The diffusivity and solubility of copper in ferromagnetic iron at lower temperatures studied by atom probe tomography.* Scripta Materialia, 2014. **83**: p. 5-8.
65. Le, T.N., et al., *Precipitation kinetics of dilute FeCu and FeCuMn alloys subjected to electron irradiation.* Scripta Materialia, 1992. **26**: p. 771-776.
66. Messina, L., et al., *Exactab initiotransport coefficients in bccFe−X(X=Cr,Cu,Mn,Ni,P,Si) dilute alloys.* Physical Review B, 2014. **90**(10).
67. Perez, M., F. Perrard, and V. Massardier, *Low-temperature solubility of copper in iron: experimental study using thermoelectric power, small angle X-ray scattering and tomographic atom probe.* Philosophical …, 2005: p. 37-41.
68. Odette, G. and B. Wirth, *A computational microscopy study of nanostructural evolution in irradiated pressure vessel steels.* Journal of nuclear materials, 1997. **251**: p. 157-171.
69. Kolli, R.P. and D.N. Seidman, *The temporal evolution of the decomposition of a concentrated multicomponent Fe–Cu-based steel.* Acta Materialia, 2008. **56**(9): p. 2073-2088.

70. Kampmann, R. and R. Wagner. *Decomposition of alloys: the early stages*. in *Proc. 2nd Acta-Scripta Metall. Conf., Pergamon, Oxford*. 1984.
71. Goodman, S., S. Brenner, and J. Low, *An FIM-atom probe study of the precipitation of copper from lron-1.4 at. pct copper. Part II: Atom probe analyses.* Metallurgical transactions, 1973. **4**(10): p. 2371-2378.
72. Mathon, M., et al., *Experimental study and modelling of copper precipitation under electron irradiation in dilute FeCu binary alloys.* Journal of nuclear materials, 1997. **245**(2): p. 224-237.
73. Russell, K.C. and L. Brown, *A dispersion strengthening model based on differing elastic moduli applied to the iron-copper system.* Acta Metallurgica, 1972. **20**(7): p. 969-974.